JOM

The Use of In-situ X-ray Imaging Methods in the Research and Development of Magnesium-based Grain-refined and Nanocomposite Materials

--Manuscript Draft--

Manuscript Number:	JOMJ-D-16-00436R1
Full Title:	The Use of In-situ X-ray Imaging Methods in the Research and Development of Magnesium-based Grain-refined and Nanocomposite Materials
Article Type:	Original Paper
Corresponding Author:	Wim Sillekens European Space Agency Noordwijk, Zuid-Hlland NETHERLANDS
Corresponding Author Secondary Information:	
Corresponding Author's Institution:	European Space Agency
Corresponding Author's Secondary Institution:	
First Author:	Wim Sillekens
First Author Secondary Information:	
Order of Authors:	Wim Sillekens
	Daniele Casari
	Wajira Mirihanage
	Sofiane Terzi
	Ragnvald Mathiesen
	Luc Salvo
	Rémi Daudin
	Pierre Lhuissier
	Enyu Guo
	Peter Lee
Order of Authors Secondary Information:	
Funding Information:	Seventh Framework Programme (FP7-NMP3-LA-2012-280421) — Not applicable
Abstract:	Metallurgists have an ever-increasing suite of analytical techniques at their disposition. Among these techniques are the in-situ methods, being those approaches that are designed to actually study events that occur in the material during for instance solidification, (thermo)-mechanical working or heat treatment. As such they are a powerful tool in unraveling the mechanisms behind these processes, supplementary to ex-situ methods that rather analyze the materials before and after their processing. In this paper, case studies are presented of how in-situ imaging methods - and more specifically micro-focus X-ray radiography and synchrotron X-ray tomography - are used in the research and development of magnesium-based grain-refined and nanocomposite materials. These results are drawn from the EC collaborative research project ExoMet (www.exomet-project.eu). The first example concerns the solidification of a Mg-Nd-Gd alloy with Zr addition to assess the role of zirconium content and cooling rate in crystal nucleation and growth. The second example concerns the solidification of a Mg-Zn-Al alloy and its SiC-containing nanocomposite material to reveal the influence of particle addition on microstructural development. The third example concerns the (partial) melting-solidification of Elektron21/AlN and Elektron21/Y2O3 nanocomposite materials to study such effects as particle

	pushing/engulfment and agglomeration during repeated processing. Such studies for one visualize and by that confirm what is known or assumed. Moreover, they advance science by monitoring and quantifying phenomena as they evolve during processing and by that contribute toward a better understanding of the physics at play.
Response to Reviewers:	The reviewer's comments on the initial version of the manuscript have been taken into account as follows. 1) The manuscript has received thorough proof-reading and editing to improve on grammar. 2) The manuscript has been restructured in separate sections on experimental procedures on the one and results and discussion on the other hand as suggested. Upon consultation with the concerned editor, track changes was not used as the heavy swapping of text would have rendered the text virtually illegible. 3) The discussion of X-ray methods has been extended by adding an additional paragraph to the introduction (paragraph 2) and by discussing the two used methods into more depth under the experimental procedures (sub-section "methods", including the schematic drawings in Figure 1 and Figure 2). The introduction of magnesium alloys as relevant materials for such studies is covered as well under the experimental procedures (sub-section "materials").

The Use of *In-situ* X-ray Imaging Methods in the Research and Development of Magnesium-based Grain-refined and Nanocomposite Materials

Sillekens W.H.[1], Casari D.[2], Mirihanage W.U.[3], Terzi S.[4], Mathiesen R.H.[2], Salvo L.[5], Daudin R.[5], Lhuissier P.[5], Guo E.[3], Lee P.D.[3]

ABSTRACT

Metallurgists have an ever-increasing suite of analytical techniques at their disposition. Among these techniques are the *in-situ* methods, being those approaches that are designed to actually study events that occur in the material during for instance solidification, (thermo)-mechanical working or heat treatment. As such they are a powerful tool in unraveling the mechanisms behind these processes, supplementary to *ex-situ* methods that rather analyze the materials before and after their processing.

In this paper, case studies are presented of how *in-situ* imaging methods – and more specifically micro-focus X-ray radiography and synchrotron X-ray tomography – are used in the research and development of magnesium-based grain-refined and nanocomposite materials. These results are drawn from the EC collaborative research project ExoMet (www.exomet-project.eu). The first example concerns the solidification of a Mg-Nd-Gd alloy with Zr addition to assess the role of zirconium content and cooling rate in crystal nucleation and growth. The second example concerns the solidification of a Mg-Zn-Al alloy and its SiC-containing nanocomposite material to reveal the influence of particle addition on microstructural development. The third example concerns the (partial) melting–solidification of Elektron21/AlN and Elektron21/Y_2O_3 nanocomposite materials to study such effects as particle pushing/engulfment and agglomeration during repeated processing.

Such studies for one visualize and by that confirm what is known or assumed. Moreover, they advance science by monitoring and quantifying phenomena as they evolve during processing and by that contribute toward a better understanding of the physics at play.

Keywords Magnesium alloys, Solidification, Grain refinement, Nanocomposites, *In situ*, X-ray imaging

[1] European Space Agency, ESTEC – Strategic & Emerging Technologies Team; PO Box 299, 2200 AG Noordwijk, NETHERLANDS (corresponding author: wim.sillekens@esa.int)
[2] NTNU Norwegian University of Science and Technology, Department of Physics; Høgskoleringen 5, 7491 Trondheim, NORWAY
[3] University of Manchester; Manchester M13 9PL, UNITED KINGDOM • Research Complex at Harwell; Didcot OX11 0FA, UNITED KINGDOM
[4] European Synchrotron Radiation Facility – Institut Laue-Langevin; EPN campus, 71 avenue des Martyrs, 38000 Grenoble Cédex, FRANCE
[5] Université Grenoble Alpes, Laboratoire SIMAP; 101 rue de la Physique, 38402 Saint Martin d'Hères Cédex, FRANCE

1 INTRODUCTION AND BACKGROUND

Metallurgists today have a huge and growing array of tools at their disposal for analysis of the materials they are investigating and developing. Traditionally, the approach in this is to study a new material (e.g., alloy chemical composition) and/or manufacturing route (e.g., casting process) by producing samples according to certain specifications and after that characterize the resulting microstructural features and (mechanical) properties so as to identify relations between those. The analytical methods for this are thus *ex situ* – Latin: "away from the (original) location", or "off-site" – meaning that the synthesis and the analysis are essentially separate activities. The issue with this is that metallurgical mechanisms like crystal nucleation and growth during solidification, recrystallization and texture development during (thermo)-mechanical working, and precipitation sequences and kinetics during heat treatment are assessed on the basis of post-mortem "snap-shots". As a result, interpretations of these mechanisms are subject to assumptions and possibly ambiguity. This triggered the development of methods that rather act *in situ* – Latin: "in the (original) location", or "on-site" – to follow events while they occur during materials processing. These methods have emerged as very promising means supplementary to the existing ones and giving an actual insight into phenomena as they evolve during for instance casting, hot extrusion and age hardening; that is, without these phenomena being masked by those that may occur at a later stage (like phase transformations, formation of intermetallic compounds, and secondary grain growth).

While the category basically covers all methods that monitor events on the spot, this paper is limited to imaging methods and more specifically even to those methods using X-rays. Hard X-rays – by their short wave lengths and high photon energies versus visual light – can penetrate otherwise opaque matter and are therefore used widely to image the inside of objects for medical and security applications, amongst others. This is of interest for metal solidification studies as well, as under appropriate conditions it enables to distinguish solid from liquid phases, and thus the crystals (grains) from the melt. By capturing consecutive images over time, the proceedings can thus be followed *in situ* and without affecting the process. The implementation of techniques designed for this purpose has been pioneered and proved successful as of late.

The results that are presented in this paper are outcomes of the ExoMet project, which is a large-scale collaborative research project that is being conducted within the 7th Framework Program of the European Commission [1]. The project (full title: "Physical processing of molten light alloys under the influence of external fields"; duration: June 2012 – July 2016; website: www.exomet-project.eu) targets high-performance aluminum- and magnesium-based materials by exploring grain-refining and nanoparticle additions in conjunction with melt treatment by electromagnetic, ultrasonic and mechanical means. These external fields are to provide for an effective and efficient dispersion of the additions in the melt and their uniform distribution in the as-cast material. The international consortium of companies, universities and research organizations integrates various disciplines as well as application areas – including automotive, aircraft, and space. Among the project partners, several are engaged in *in-situ* imaging investigations, of which selected examples relating to magnesium-based materials are presented below. The objective of this paper is thus to demonstrate how these methods can be used in support of the research and development of such materials.

A common aspect in the study of grain-refined and nanocomposite materials is the presence or formation of particles in an alloy melt. These particles are to serve as inoculants for crystal nucleation, or as reinforcements of the solidified matrix, respectively. While they are typically micrometer- to nanometer-sized, their interaction with the alloy during solidification may distinctly affect microstructural development (i.e., as compared to that in the monolithic alloy). The case studies below will illustrate this point. To start off with, however, the used materials and methods are introduced.

2 EXPERIMENTAL PROCEDURES

2.1 Materials

Magnesium is being used for structural applications such as for automotive components because of its weight-saving potential (being 35% lighter than aluminum and 75% lighter than steel). Magnesium alloys are commonly applied as shape castings, using such processes as high-pressure die casting and sand casting for their manufacturing.

To study the solidification behavior with X-ray imaging methods, the contrast between the solid and liquid phases needs to be adequate. This depends on the phases' differences in chemical composition and density. As it happens, this prerequisite is met for the commercial alloy Elektron21, which is a magnesium alloy with rare-earth alloying elements. Alternatively, one may turn to model alloys that contain an alloying element that is just added to provide this contrast, such as zinc. Both options are used in the studies at hand. Ceramic particles generally provide for adequate contrast with a magnesium melt and can be imaged, provided that they are not too small.

2.2 Methods

For the *in-situ* X-ray imaging studies at hand, some distinctly different imaging principles and instruments were used.

Micro-focus X-ray radiography was employed at NTNU Norwegian University of Science and Technology. Figure 1 shows a schematic of the set-up. The laboratory-based configuration consists of a micro-focus X-ray source, a tailored Bridgman-type gradient furnace, and a dedicated X-ray detector [2]. The facility was adapted for the study of magnesium-based materials by integrating an environmentally controlled chamber to prevent self-ignition of the samples via argon insertion [3]. Samples and their holders are encased between two X-ray transparent glassy carbon plates to avoid any other reactions between molten magnesium and its surroundings. Grain buoyancy and thermo-solutal convection are minimized by orienting the sample cell horizontally; that is, with gravity acting in sample thickness direction. The operating parameters of the X-ray source can be tuned to provide the best compromise between sample transmission and absorption contrast. In a typical solidification experiment, the heating by both elements is adjusted until equi-axed nucleation occurs close to the center of the field of view (FoV), indicating a nearly isothermal condition. A spatial resolution down to 5 µm can be achieved for usual image-capturing rates of 3 Hz. The collected data are subsequently post-processed by means of flat-fielding, noise-filtering and edge-sharpening techniques.

Synchrotron X-ray tomography was employed at Diamond Light Source, UK (Diamond-Manchester imaging beamline I13-2) and at the European Synchrotron Radiation Facility, France (beamline ID19). Figure 2 shows a schematic of the set-up at the latter site. The sample is contained in an argon-filled quartz capillary (to avoid reaction with oxygen and by that self-ignition of the sample), which is fixed on an alumina rod and mounted on a rotating stage. An induction coil is used to heat the samples; the temperature is monitored through a pyrometer and controlled by manually adjusting power supply to the electric generator. The high brilliance of the X-ray source allows for very fast imaging. Thus, numerous projections are recorded by the detector system as the stage rotates, from which afterwards 3D images can be reconstructed by numerical treatment. Details of the two employed tomography set-ups differ somewhat, as is specified in the concerned sub-sections below.

Associated with the differences in the used imaging principles and instruments, there are also differences in the capabilities of the two methods [4]. Where micro-focus X-ray radiography can be implemented as a stand-alone facility and be based for most on commercially available X-ray sources and other components, synchrotron X-ray tomography requires access to one of the few dedicated large-scale facilities. As the names further suggest, radiography provides projections (2D) and tomography provides spatial information (3D).

3 CASE STUDIES

3.1 Solidification of a Mg-Nd-Gd alloy with Zr addition

An important class of magnesium alloys uses rare-earth alloying elements for the purpose of enhancing mechanical properties and notably creep resistance. For these alloys, zirconium is commonly added up to saturation level as a potent grain refiner, meaning that it promotes grain nucleation upon solidification which then leads to a correspondingly finer and more favorable microstructure.

The solidification experiments that are reported here were designed to study the grain-refinement mechanism induced by the presence of zirconium in these alloys. Micro-focus X-ray radiography was used as it enables multiple experiments to be done to explore the influence of such parameters as cooling rate and with still sufficient spatiotemporal resolution to distinguish the main morphological features. Two alloy variants based on the Elektron21 alloy were employed (chemical composition 2.8 wt.% Nd, 1.5 wt.% Gd, balance Mg, which is in line with the commercial equivalent except for the addition of Zn). Zr was added in unsaturated and supersaturated concentrations of 0.35 wt.% and 0.86 wt.%, respectively. For these experiments at NTNU Norwegian University of Science and Technology, samples were prepared by sectioning 50×5×1 mm strips from the as-cast ingots, and manually grind them with progressively finer silicon carbide paper (up to 4000 grit) to reach final dimensions of 50×5×0.20(1) mm.

Figure 3 shows the effect of zirconium addition level on the development of the α-Mg grains for a relatively low cooling rate. As time proceeds – and temperature drops – the grains that appear in bright contrast are growing with a typical six-fold symmetry associated with the hexagonal closed-packed crystal lattice of magnesium. In the alloy with high Zr content, the number of nucleation events is 1.5–2 times higher than in the alloy with low Zr

content. Upon closer examination of the images for the supersaturated alloy, one also detects several dark spots in the melt just ahead of the solid/liquid interface. These could be either pre-existing zirconium particles pushed by the growing grains, or new particles forming through a secondary peritectic reaction in the enriched liquid between neighboring grains. Interestingly – despite being several micrometers in size – these particles appear not to promote any further nucleation and are eventually trapped in the eutectic regions between α-Mg grains.

For further comparison, average grain size *d* after solidification has been estimated as:

$$d = \left(\frac{6}{\pi N_0}\right)^{1/3}, \quad (1)$$

where N_0 is the grain density; i.e., the number of counted grains divided by the FoV volume (~1.11 mm^3). For the alloy with low Zr content, resulting values are 370, 245 and 200 µm for imposed cooling rates of 0.0125, 0.05 and 0.1 K/s, respectively. For the alloy with high Zr content, the matching values are 290, 210 and 170 µm. This confirms that a higher zirconium addition level indeed enhances grain refinement, as well as that a higher cooling rate leads to finer grains. The last-mentioned grain-size value in this set appears to be in fair agreement with earlier grain-refinement efficiency tests using a Mg-Nd-Zn alloy [5]. Further, it is to be noted that grain-size dependence on cooling rate is more pronounced for the alloy with the low grain-refiner addition level, similar to results reported earlier for alloys based on the Al-Cu system [6].

Finally, solid-area fraction data from these experiments are presented in Figure 4. For a given cooling rate, the alloy with high Zr content generally exhibits a higher rate of solid formation than the alloy with low Zr content, which then results in a generally higher solid-area fraction. For the higher cooling rates, solidification sets in at higher undercooling, suggesting the presence of a higher number of Zr particles becoming potent only if a sufficiently high undercooling is reached. This is in accordance with the so-called Free-Growth model [7]. A subsequent decrease in the rate of solid formation is noted for the alloys solidifying at 0.05 and 0.1 K/s, occurring almost at a same undercooling of ~1.25 K and ~1.5 K, respectively: no further grain nucleation is observed in the images at these stages. The alloy with high Zr content solidifying at 0.0125 K/s behaves similarly, tilting at ~0.7 K. In contrast, the curve for the alloy with low Zr content at this cooling rate evolves almost linearly, which can be interpreted as near-equilibrium solidification.

3.2 Solidification of a Mg-Zn-Al alloy and its SiC-containing nanocomposite material

One of the main challenges in the melt-metallurgical synthesis of nanocomposites is in achieving a uniform distribution of the particles in the as-cast material. This relates to the introduction of the particles in the melt, but also to the interaction between particles and the solid-liquid interface during solidification. As for the latter, the presence of particles may also affect the morphology of the growing grains.

The solidification experiments that are reported here were designed to study the effects of nanoparticles on the primary dendritic microstructural evolution. Synchrotron X-ray tomography was used as it enables to capture moving solid-liquid interfaces through reasonably good phase contrast. Material was prepared by blending magnesium alloy AZ91 with pure zinc so as to obtain a model alloy of specific chemical composition (25 wt.% Zn, 7 wt.% Al, balance Mg). Nanocomposite samples were then synthesized by adding 0.7 wt.% SiC

powder (average particle size ~25 nm) applying ultrasound to the melt before casting to enhance particle dispersion. For these experiments at Diamond Light Source, ∅1.2 mm cylindrical samples are extracted from the ingots and then encapsulated by graphite and quartz tubes.

Figure 5 shows results for the solidification of the monolithic alloy (top) and the composite material (bottom). These 2D transverse slices were constructed from the 3D tomographic images obtained at distinct points in time, and thus at distinct points during solidification. The cooling rate was set to be quite low to get low growth rates and by that enhance image quality (solid-liquid movement during the acquisition of a single tomographic image may induce image blurring). It is to be noted that individual particles as well as actual crystal nucleation cannot be recognized due to the limited spatiotemporal resolution. Further, grains below some micrometers of size will be beyond detection as for the limited absorption difference. The slices at the far left of the figure are those for which first signs of dendrites are observed; these emerge in dark contrast. Upon comparing the chronological images, it appears that the composite material shows enhanced nucleation and reduced growth rate versus the monolithic alloy. Smaller average grain size results after solidification: 235±35 µm for the alloy with particles as compared to 300±50 µm for the one without particles. From literature it is known that the α-Mg growth pattern can be remarkably influenced by the characteristics of the surrounding melt [8]. That submicron-sized particles in a solidifying melt can either be engulfed or pushed by the moving solidification front is also recognized. Due to their generally poor wettability by a metal melt and their large surface-to-volume ratio, uniform dispersion of nanoparticles is challenging. Clustering is commonly observed and tried to be countered by melt-processing methods such as ultrasonic treatment [9–11]. From this it seems reasonable that particle pushing during primary dendritic phase solidification needs to be assumed for the experiments at hand. Earlier work also suggests that phase growth can be affected by nanoparticle self-assembly ahead of the solidification front [12, 13]. Such accumulation can act as a barrier to diffuse solute (rejected at the solid-liquid interface) away from the advancing solidification front, introducing higher local enrichment close to the solid-liquid interface as compared to regular solidification conditions. That in turn can retard phase growth. Also, lower solute enrichment in the bulk liquid caused by higher local enrichment close to the solid-liquid interface can permit higher undercooling, increasing nucleation potential. Both mechanisms may lead to microstructural refinement, as observed in the current experiments.

3.3 Melting–solidification of Elektron21/AlN and Elektron21/Y_2O_3 nanocomposite materials

Interactions between particles and the melt upon solidification can apparently affect grain morphology (as discussed in the previous case study), but may also lead to non-uniform particle distributions in the as-cast material such as particle clusters on the grain boundaries. This also poses the question how these interactions extend and affect eventual material quality when multiple melting and solidification steps are involved, like in recycling.

The (partial) melting and subsequent solidification experiments that are reported here were designed to study the evolution of particle distribution as well as to detect and observe any reactions of particles with the melt. As yet, most of the experimental data available on these issues are based on post-mortem observations of quenched samples [14–17], or on *in-situ* 2D experiments performed using transparent organic alloys [18–20].

Synchrotron X-ray tomography was used here as it enables 3D real-time observation with actual metallic alloys, thus avoiding potential bias introduced by the experimental limitations in these earlier studies. Two metal-matrix nanocomposite materials were employed, both based on the Elektron21 alloy. To the base alloy (chemical composition 2.8 wt.% Nd, 1.2 wt.% Gd, 0.3 wt.% Zn, 0.4 wt.% Zr, balance Mg), either 1 wt.% AlN (average particle size 20–30 nm) or 1 wt.% Y_2O_3 (average particle size ~500 nm) were added, applying ultrasound to the melt before casting to enhance particle dispersion [21]. For these experiments at the European Synchrotron Radiation Facility, ∅1×5 mm cylindrical samples were machined from the as-received ingot and encapsulated by a quartz tube under argon atmosphere.

Figure 6 presents results obtained from a partial melting experiment on an Elektron21/AlN sample. Images (a) and (b) are 2D transverse slices extracted from the 3D tomographic images in the solid and the partially molten state, respectively. In (a), the rare-earth rich eutectic appears in bright contrast while the α-Mg grains appear in dark contrast. Upon reaching the eutectic temperature, the intermetallic phases located in the interdendritic regions start melting. In (b), temperature has further increased, revealing that the α-Mg phase coarsens and its initial dendritic morphology becomes more globular. Simultaneously the solid fraction has decreased and the contrast of the liquid phase has become less bright. Further, it appears that some liquid droplets nucleate and grow inside the grains, which follows a mechanism discussed elsewhere [23]. Moreover, bright white spots emerge as is obvious from (c), which is a larger magnification of the sample at the same temperature. Metallography has revealed that in this composite material the AlN particles are coated by a Zr-rich layer [21], possibly ZrN [24, 25], and mainly appear as micrometer-sized clusters. In some cases, this layer grows into a larger phase, also rich in heavy elements but with a possibly different structure and composition. It is therefore believed that the observed bright white spots are small clusters of AlN particles coated by a Zr-rich layer and possibly embedded in a third phase that has grown from the particle surface. The heavy elements in these heterogeneous and compact clusters then act as markers, revealing the presence of the actual AlN particles. From the image it is clear that the particles/clusters are located at the solid-liquid interface as well as within the α-Mg phase. While it cannot be ruled out that the particles moved from the former to the latter during melting, this is nevertheless a strong indication that these particles have been there in the as-received state and thus have been engulfed upon initial solidification. The Zr-rich layer on the AlN particles may be instrumental in creating a favorable interface condition for such engulfment. Finally, (d) shows a 3D rendering of the particle distribution in the partially molten state, being indicative for the efficiency of the original dispersion process. The distribution seems fairly uniform at the sample scale, with most particles appearing as micrometer-sized heterogeneous clusters containing heavy elements. As particles in a melt tend to agglomerate in the absence of stirring, it appears likely that particle distribution in the as-received sample has been even more uniform than after its partial re-melting.

Figure 7 shows results from the same experiment during its successive re-solidification stage. Clearly the bright phase forming from the AlN particle surface grows when it gets in contact with the liquid phase, which is locally enriched in solute. The exact structure and composition of this growing phase is still to be determined. Nevertheless, it is apparent that additional complexity is introduced to the exploration of (nano)-composite materials as particles may be reacting with the melt during their processing.

Figure 8 presents results obtained from a full melting and subsequent solidification experiment on an Elektron21/Y_2O_3 sample, showing 2D longitudinal slices (top) and the

corresponding 3D renderings of the particles (bottom) at successive time steps. This particular composite system has proven to be stable; i.e., the ceramic particles do not react in contact with the magnesium-alloy melt. After completely melting the matrix (images at the far left of the figure), most of the particles have settled at the bottom of the sample. Yet, some large clusters ended up at the sample wall (its oxide skin appears bright in these images), so that their interaction with the solidification front during cooling could be observed. During cooling a thermal gradient was present with solidification progressing from the bottom of the sample to the top. It appears that some particles are pushed away from the sample wall as the solidification front passes. The observation of large particle clusters being pushed by growing dendrites was recently reported for an aluminum-based nanocomposite material [26]. Here, particle clusters remained in the re-molten state as stable branched networks (coinciding with the original grain boundaries) that turned out to be difficult to break up. In the present case, however, pushing goes along with cluster fragmentation and some particles are transported far from their original location at the sample wall. Further analyses and additional tests are ongoing to shed light on the mechanisms involved.

4 CONCLUSION AND OUTLOOK

In this paper it is shown that *in-situ* imaging methods such as micro-focus X-ray radiography and synchrotron X-ray tomography can be used to study microstructural features of magnesium-based grain-refined and nanocomposite materials and local mechanisms involved during their melt-metallurgical processing.

Results for one visualize and by that confirm what is known or assumed. Examples are that magnesium crystals upon solidification grow in a six-fold symmetry, that higher cooling rates during solidification lead to finer microstructures, and that zirconium is a potent grain refiner in magnesium rare-earth alloys. Moreover, they provide for additional insight by enabling to monitor and quantify phenomena and by that contribute toward a better understanding of the physics at play. Examples are that nanoparticles despite their size can affect the morphology of the growing grains during solidification, that engulfment and/or pushing of particles by the solidification front may or may not occur depending on the specifics of the system, and that chemical reaction at the solidification front may induce the formation of new particles. While the former serves the general understanding and can be used for educational purposes, the latter is an enabler for enhancing scientific understanding and supporting technological development to be of eventual benefit for industrial applications.

There are restrictions in the use of these methods nevertheless. The number of synchrotron facilities is limited, so access is a concern along with the need for specific expertise, the long lead times and the limited operational flexibility of the experimental campaigns. Further, concessions may have to be done on alloy compositions (regarding the necessary contrast) and the design of experiments (e.g., at the expense of duplication trials). Nowadays tomography imaging detectors (cameras) with very high acquisition rates are used, leading to huge amounts of collected data, while for other techniques such as diffraction the increasing use of 2D detectors poses a similar challenge. Thus there is an extensive effort to be made on the storage, transfer, processing and analysis of these data. Data management in practice is one of the main concerns, especially in regard of non-expert

users. For solidification studies, there still are technical constraints such as on the attainable resolution and field of view of the images versus the features to be studied, and in setting experimental conditions possibly close to those in practice. The former would imply a smaller beam and/or better optics and wider detectors. The latter would imply larger sample volumes and faster cooling rates, meaning higher energies and higher acquisition frequencies (i.e., higher photon fluxes), respectively. Developments like these are indeed being considered in topical upgrading programs at existing facilities including the European Synchrotron Radiation Facility. Recapitulating, for the foreseeable future it is not expected that especially synchrotron studies will become more economical, but faster and more accurate and only better accessible if post-processing becomes easier. They thus remain to be regarded as high-gain techniques supplementary to those in the metallographical laboratory. In the laboratory, *in-situ* studies will become more common as capabilities of laboratory tomography systems, small-angle X-ray scattering devices and so on further evolve. Moreover, the more "conventional" *ex-situ* characterization techniques remain crucial in their own right, yet also for the preparation and evaluation of *in-situ* studies.

ACKNOWLEDGEMENTS

The authors wish to acknowledge financial support from the ExoMet project, which is co-funded by the European Commission in the 7th Framework Program (contract FP7-NMP3-LA-2012-280421), by the European Space Agency and by the individual partner organizations. Among the consortium, Helmholtz-Zentrum Geesthacht (MagIC), Germany, is thanked for the provision of the magnesium rare-earth testing materials.

Diamond Light Source – Research Complex at Harwell, United Kingdom, is acknowledged for the use of the Diamond-Manchester branch-line under experiment MT11837-1 and the support from the I13 team. The European Synchrotron Radiation Facility, France, is acknowledged for the allocation of beam-time in the framework of the proposals MA-2984 and LTP MA1876 and the strong support by the ID19 beamline team.

REFERENCES

1. W.H. Sillekens, D.J. Jarvis, A. Vorozhtsov, V. Bojarevics, C.F. Badini, M. Pavese, S. Terzi, L. Salvo, L. Katsarou, and H. Dieringa, *Metall. Mater. Trans. A*, **45A**, 3349 (2014).
2. A.G. Murphy, D.J. Browne, W.U. Mirihanage, and R.H. Mathiesen, *Acta Mater.*, **61**, 4559 (2013).
3. D. Casari, W.U. Mirihanage, K.V. Falch, I.G. Ringdalen, J. Friis, R. Schmid-Fetzer, D. Zhao, Y. Li, W.H. Sillekens, and R.H. Mathiesen, *Acta Mater*., **116** 177 (2016).
4. C. Rakete, C. Baumbach, A. Goldschmidt, D. Samberg, C.G. Schroer, F. Breede, C. Stenzel, G. Zimmermann, C. Pickmann, Y. Houltz, C. Lockowandt, O. Svenonius, P. Wiklund, and R.H. Mathiesen, *Rev. Sci. Instrum.*, **82**, 105108 (2011).
5. C. Wang, M. Sun, F. Zheng, L. Peng, and W. Ding, *J. Magnesium and Alloys,* **2**, 239 (2014).
6. A.G. Murphy, W.U. Mirihanage, D.J. Browne, and R.H. Mathiesen, *Acta Mater.*, **95**, 83 (2015).

7. A.L. Greer, A.M. Bunn, A. Tronche, P.V. Evans, and D.J. Bristow, *Acta Mater.*, **48**, 2823 (2000).
8. M.Y. Wang, Y.J. Xu, T. Jing, G.Y. Peng, Y.N. Fu, and N. Chawla, *Scripta Mat.*, **67**, 629 (2012).
9. R. Casati, *Aluminum Matrix Composites Reinforced with Alumina Nanoparticles*, 1st ed. (Springer, 2016), pp. 9–15, 27–28, 59–72.
10. X. Li, Y. Yang, and X. Cheng, *J. Mater. Sci.*, **39**, 3211 (2004).
11. W. Mirihanage, W. Xu, J. Tamayo-Ariztondo, D. Eskin, M. Garcia-Fernandez, P. Srirangam, and P. Lee, *Mater. Lett.*, **164**, 484 (2016).
12. L. Chen, J. Xu, H. Choi, H. Konishi, S. Jin, and X. Li, *Nat. Commun.*, **5**, 3879 (2014).
13. L. Chen, J. Xu, and X. Li, *Mater. Res. Lett.*, **3**, 43 (2015).
14. F.R. Juretzko, D.M. Stefanescu, B.K. Dhindaw, S. Sen, and P.A. Curreri, *Metall. Mater. Trans. A*, **29**, 1691 (1998).
15. Y.M. Youssef, R.J. Dashwood, and P.D. Lee, *Compos. Part. A: Appl. Sci. Manuf.*, **36**, 747 (2005).
16. T. Lierfeld, P. Gandham, M. Kolbe, T. Schenk, H.M. Singer, G. Eggeler, and D.M. Herlach, *Mater. Sci. Eng. A*, **449–451**, 689 (2007).
17. D.M. Stefanescu, B.K. Dhindaw, S.A. Kacar, and A. Moitra, *Metall. Trans. A*, **19**, 2847 (1988).
18. D.R. Uhlmann, B. Chalmers, and K.A. Jackson, *J. Appl. Phys.*, **35**, 2986 (1964).
19. J.A. Sekhar and R. Trivedi, *Mater. Sci. Eng. A*, **147**, 9 (1991).
20. D.M. Stefanescu, F.R. Juretzko, A. Catalina, B.K. Dhindaw, S. Sen, and P.A. Curreri, *Metall. Mater. Trans. A*, **29**, 1697 (1998).
21. L. Katsarou, M. Mounib, W. Lefebvre, S. Vorozhtsov, M. Pavese, C. Badini, J.M. Molina-Aldareguia, C.C. Jimenez, M.T. Pérez Prado, and H. Dieringa, *Mater. Sci. Eng. A*, **659**, 84 (2016).
22. D. Paganin, S.C. Mayo, T.E. Gureyev, P.R. Miller, and S.W. Wilkins, *J. Microsc.*, **206**, 33 (2002).
23. S. Terzi, L. Salvo, M. Suéry, A.K. Dahle, and E. Boller, *J. Mater. Sci.*, **48**, 7422 (2013).
24. A. Koltsov, F. Hodaj, N. Eustathopoulos, A. Dezellus, and P. Plaindoux, *Scr. Mater.*, **48**, 351 (2003).
25. R.E. Loehman and A.P. Tomsia, *Acta Metall. Mater.*, **40**, S75 (1992).
26. R. Daudin, S. Terzi, P. Lhuissier, L. Salvo, and E. Boller, *Mater. Des.*, **87**, 313 (2015).

FIGURE CAPTIONS

Figure 1 Micro-focus X-ray radiography: experimental set-up in the NTNU home-lab (Viscom Vision Technology XT9100 X-ray source, ① sample, ② heater element, ③ adiabatic zone, ④ field of view, ⑤ projected image, ⑥ Vosskuhler DXI-11000 CCD camera equipped with a Scint-X scintillator).

Figure 2 Synchrotron X-ray tomography: experimental set-up on the ESRF–ID19 beamline (① sample, ② quartz capillary, ③ alumina rod, ④ rotation stage, ⑤ induction coil, ⑥ pyrometer, ⑦ scintillator, ⑧ optics system, ⑨ PCO Dimax camera).

Figure 3 Microstructural evolution during solidification of Elektron21-based alloys with different zirconium contents C_{Zr} – cooling rate CR=0.0125 K/s (experimental: thermal cycling with cooling from 943 K; imaging: micro-focus X-ray radiography, beam energy 40 keV and 50 µA, field of view 2,817×1,848 µm, virtual pixel size ~1.4 µm, image-capturing rate 1 Hz).

Figure 4 Solid-area fraction in dependence on the undercooling ΔT during solidification of Elektron21-based alloys with different zirconium contents C_{Zr} and for different cooling rates CR (experimental and imaging: as for Figure 3, with solid grain envelopes measured using a manual grey-level thresholding of the images).

Figure 5 Microstructural evolution during solidification of a Mg-25Zn-7Al alloy and a Mg-25Zn-7Al/SiC nanocomposite material – from left to right: at 635 K, at 622 K, at 604 K, at 577 K, and at 532 K (experimental: cooling from ~665 K at 0.05 K/s; imaging: synchrotron X-ray tomography, polychromatic beam, beam energy 8–30 keV, 1200 projections over 180° rotation per tomographic image, exposure time 10 ms/projection, distance sample–scintillator ~10 cm, 1.6 µm effective spatial resolution with a 1280×1080 pixel imaging array).

Figure 6 Microstructural evolution during melting of an Elektron21/AlN nanocomposite material: (a) as-received state at 293 K, (b–d) semi-solid state at 875 K (experimental: heating at 0.1 K/s; imaging: synchrotron X-ray tomography, beam energy 9.6 keV, 800 projections over 180° rotation, time scan ~1 s, field of view 816×816×406 voxels, voxel size 1.1 µm, Paganin 3D image reconstruction [22]).

Figure 7 Particle reaction during solidification of an Elektron21/AlN nanocomposite material: (a) at 873 K, (b) at 863 K, (c) at 841 K, (d) at 806 K, and (e) solidified state, including a 3D rendering of the phase morphology (experimental: partial melting, then cooling from 878 K at 0.1 K/s; imaging: as for Figure 6).

Figure 8 Pushing and fragmentation of particle clusters during solidification of an Elektron21/Y_2O_3 nanocomposite material (experimental: cooling from liquid state at 1 K/s; imaging: synchrotron X-ray tomography, beam energy 9.6 keV, 800 projections over 180° rotation, time scan ~3 s, field of view 816×816×816 voxels, voxel size 1.1 µm, Paganin 3D image reconstruction).

Figure 1

Click here to download Figure Figure 01.tif

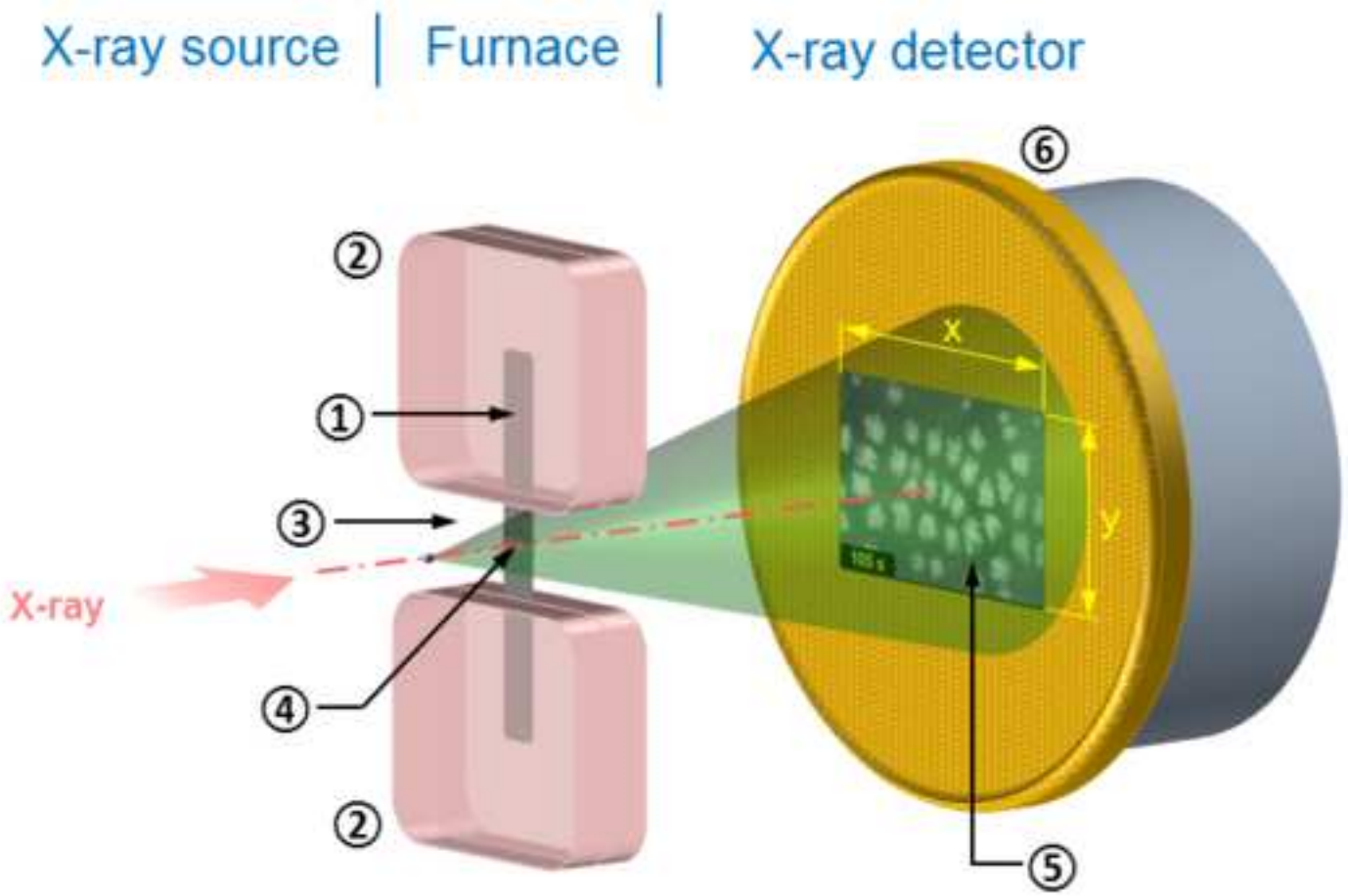

Figure 2

Click here to download Figure Figure 02.tif

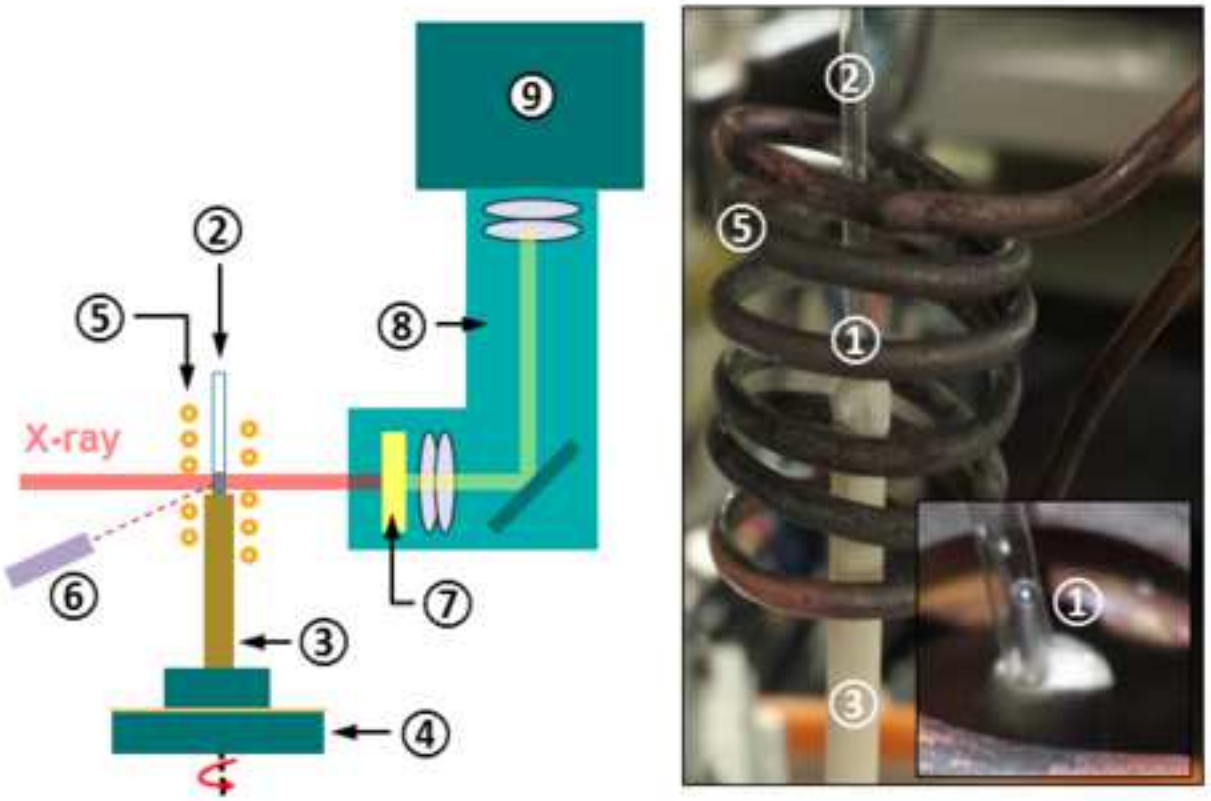

Figure 3

Click here to download Figure Figure 03.tif

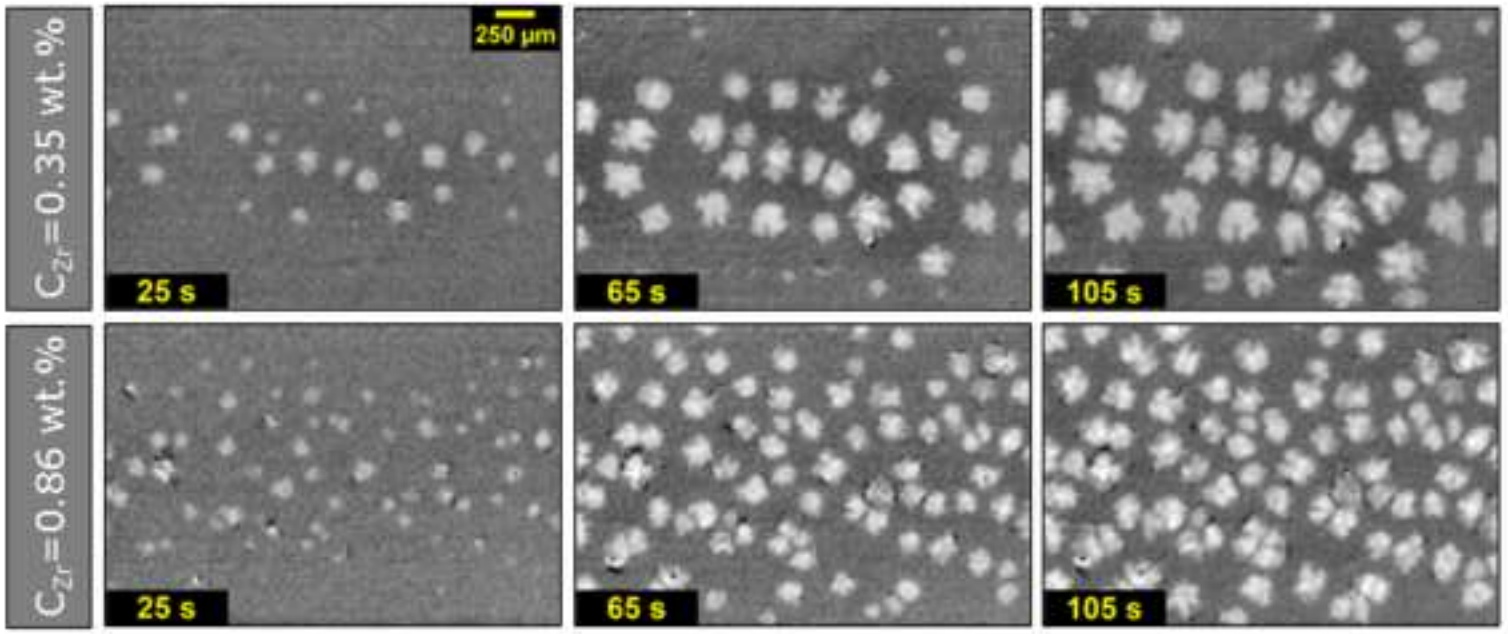

Figure 4

Click here to download Figure Figure 04.tif

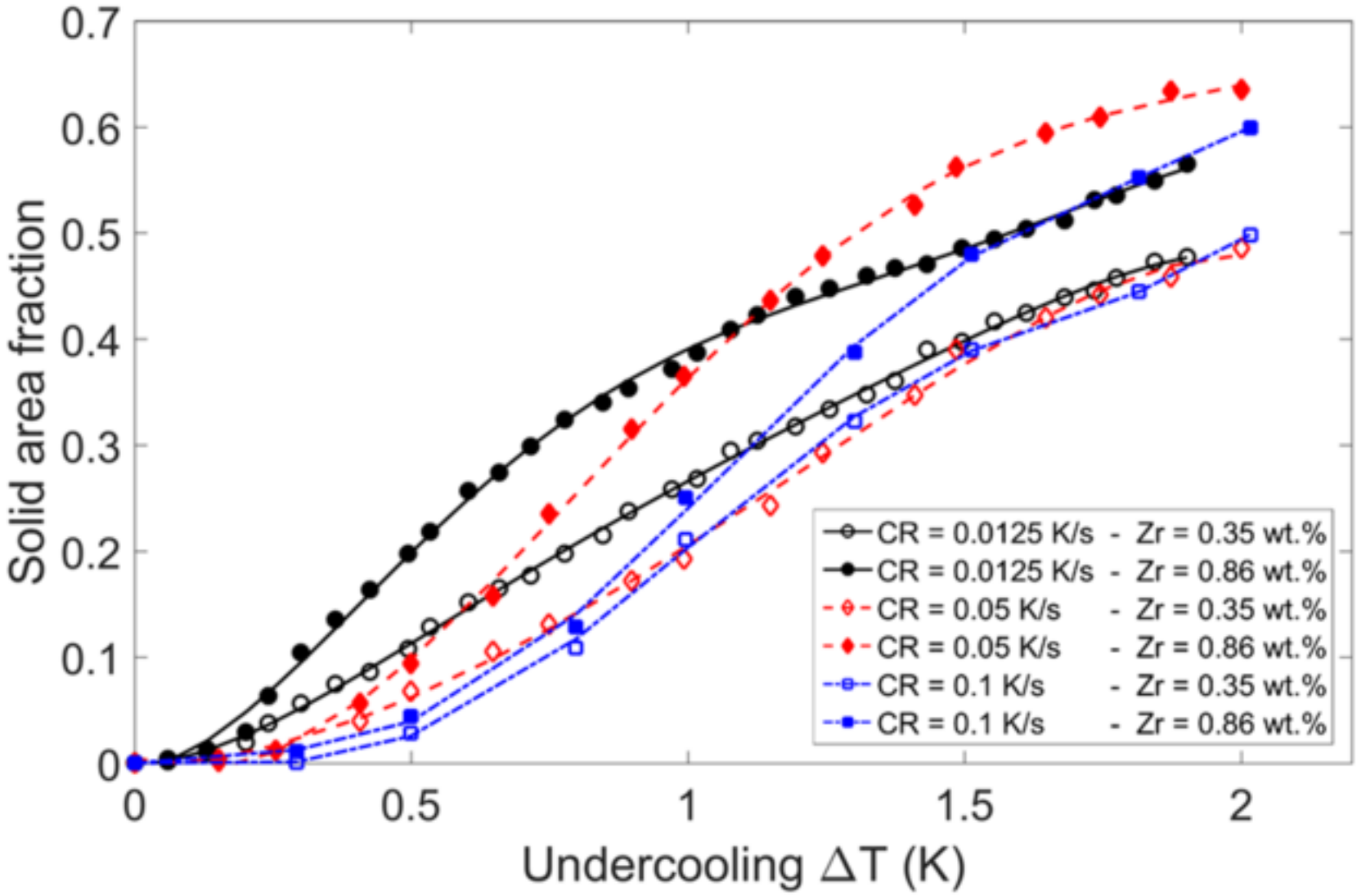

Figure 5

Click here to download Figure Figure 05.tif

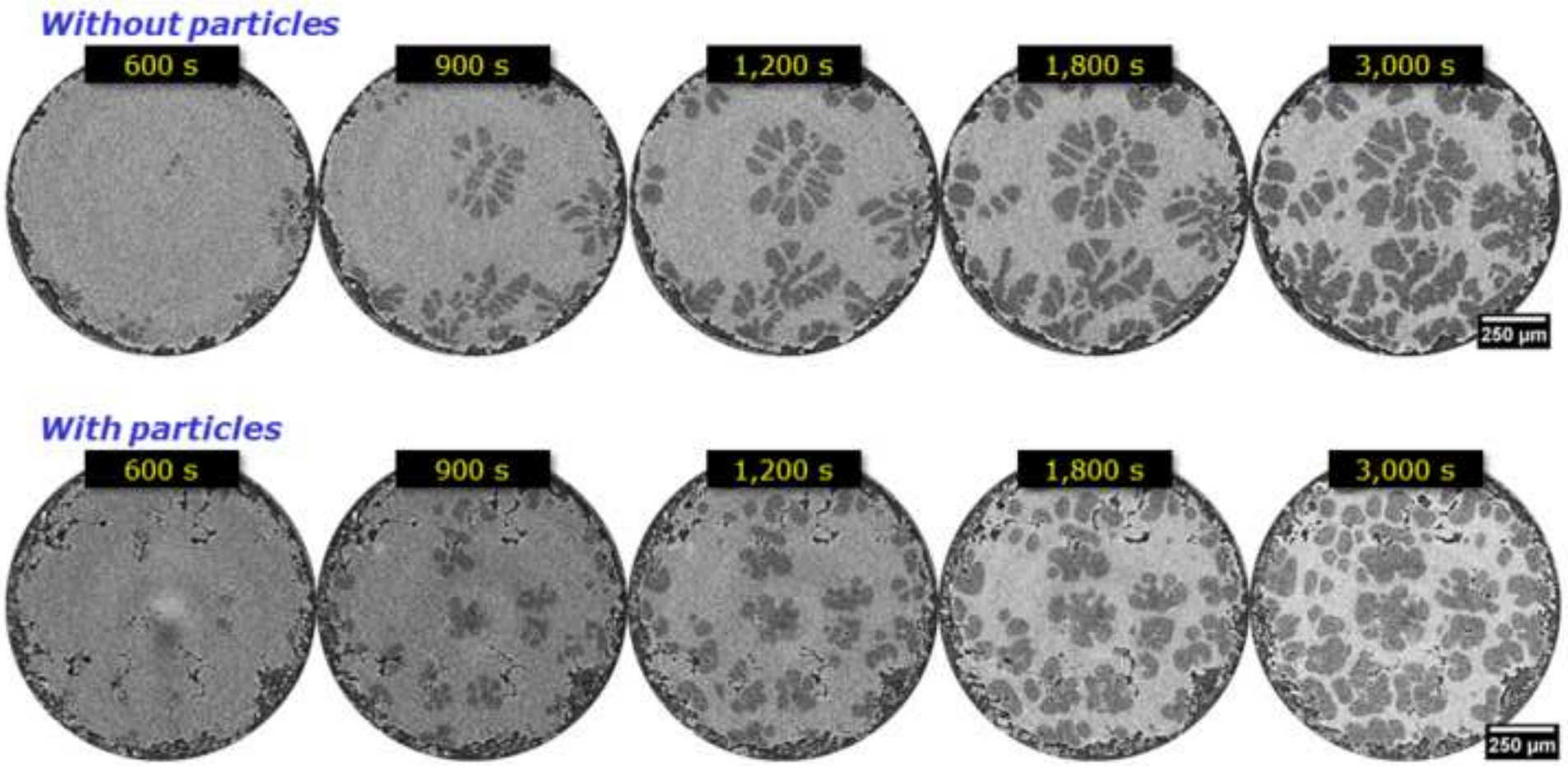

Figure 6

Click here to download Figure Figure 06.tif

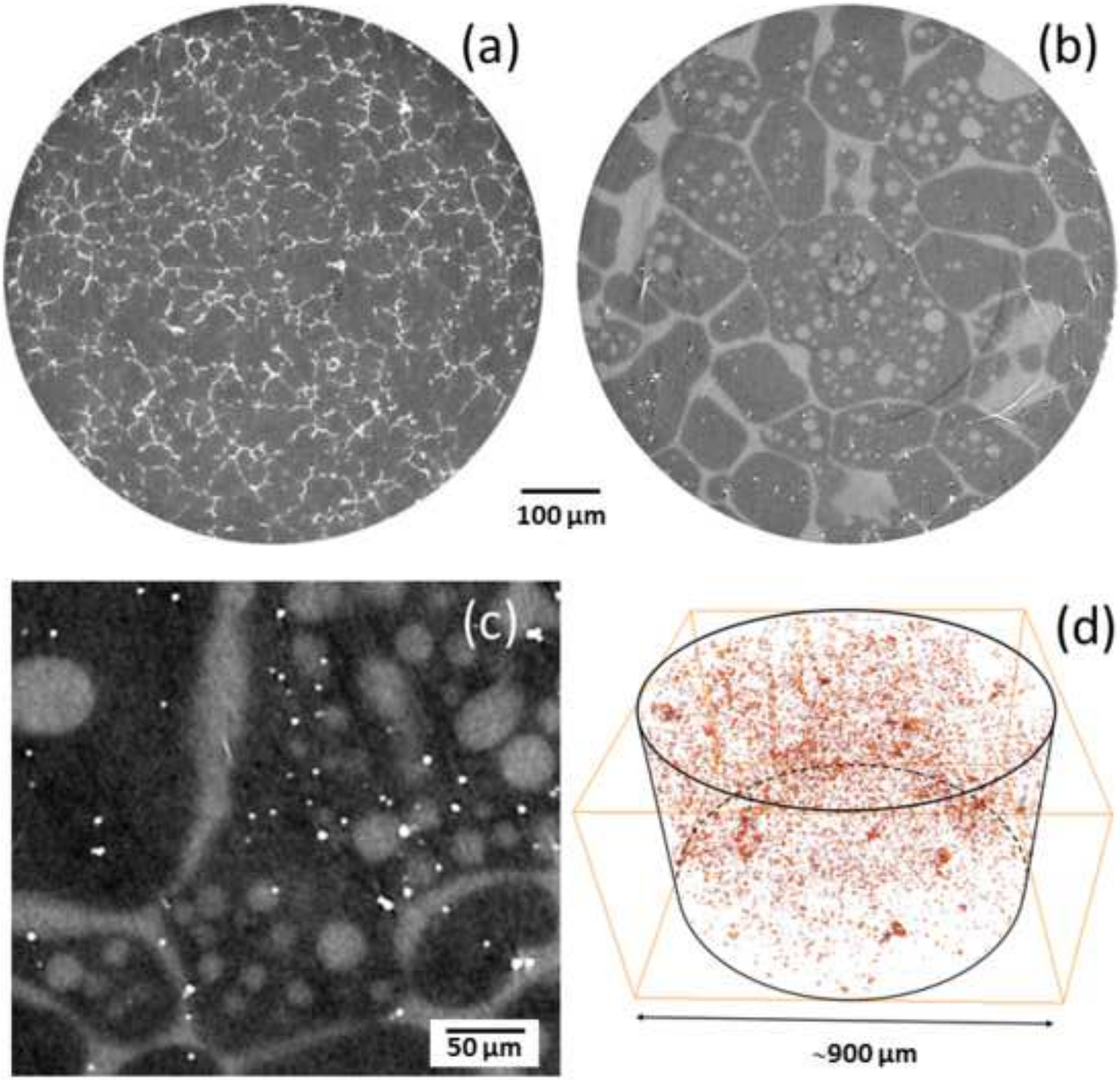

Figure 7

Click here to download Figure Figure 07.tif

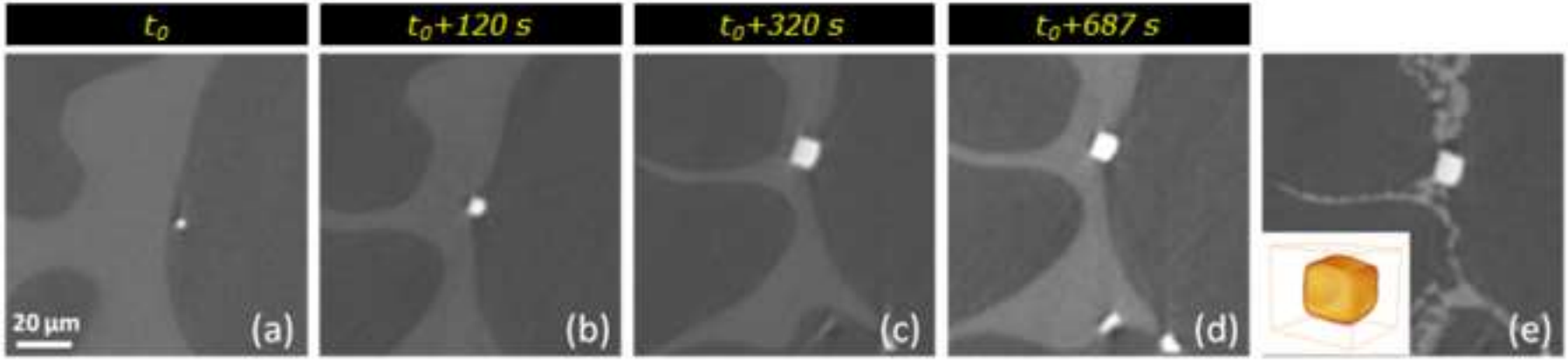

Figure 8

Click here to download Figure Figure 08.tif

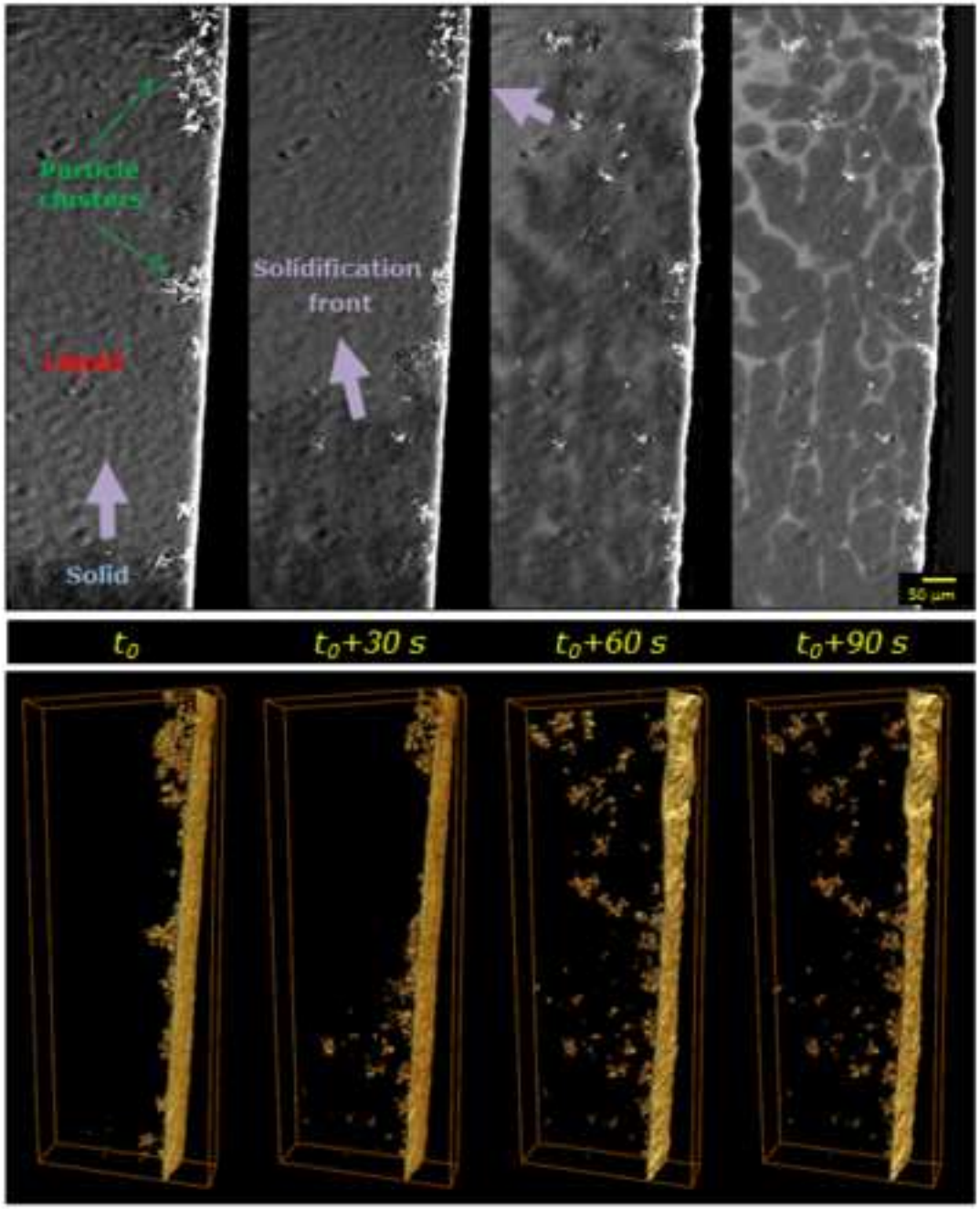

The Use of *In-situ* X-ray Imaging Methods in the Research and Development of Magnesium-based Grain-refined and Nanocomposite Materials

Sillekens W.H.[1], Casari D.[2], Mirihanage W.U.[3], Terzi S.[4], Mathiesen R.H.[~~3~~2], Salvo L.[5], Daudin R.[5], Lhuissier P.[5], Guo E.[3], Lee P.D.[3]

ABSTRACT

Metallurgists have an ever-increasing suite of analytical techniques at their disposition ~~for materials research and engineering.~~. Among these techniques are the *in-situ* methods, being those approaches that are designed to actually study events that occur in the material during for instance solidification, (thermo)-mechanical working or heat treatment. As such they are a powerful tool in unraveling the mechanisms behind these processes, supplementary to *ex-situ* methods that rather analyze the materials before and after their processing.

In this ~~contribution, examples~~paper, case studies are presented of how *in-situ* imaging methods – and more specifically micro-focus X-ray radiography and synchrotron X-ray tomography – are used in the research and development of magnesium-based grain-refined and nanocomposite materials. These results are drawn from the EC collaborative research project ExoMet (www.exomet-project.eu). The first example concerns the solidification of a Mg-Nd-Gd alloy with Zr addition to assess the role of zirconium content and cooling rate in crystal nucleation and growth ~~by micro-focus X-ray radiography.~~. The second example concerns the solidification of a Mg-Zn-Al alloy and its SiC-containing nanocomposite material to reveal the influence of particle addition ~~and cooling rate~~ on microstructural development ~~by synchrotron X-ray tomography.~~. The third example concerns the (partial) ~~re-~~melting ~~and -~~solidification of Elektron21/AlN and Elektron21/Y_2O_3 nanocomposite materials to study such effects as particle pushing/engulfment and ~~clustering~~agglomeration during repeated processing ~~(e.g., recycling) by synchrotron X-ray tomography~~.

~~While these results~~Such studies for one visualize and by that confirm what is known or assumed. Moreover, they ~~moreover~~ advance science by ~~following~~monitoring and quantifying phenomena as they evolve during processing and by that contribute toward a better understanding of the physics at play.

Keywords ~~magnesium~~Magnesium alloys, ~~solidification, grain~~Solidification, Grain refinement, ~~nanocomposites, in-~~Nanocomposites, *In situ*, X-ray imaging

[1] European Space Agency, ESTEC – Strategic & Emerging Technologies Team; PO Box 299, 2200 AG Noordwijk, NETHERLANDS (corresponding author: wim.sillekens@esa.int)
[2] NTNU Norwegian University of Science and Technology, Department of Physics; Høgskoleringen 5, 7491 Trondheim, NORWAY
[3] University of Manchester; Manchester M13 9PL, UNITED KINGDOM • Research Complex at Harwell; Didcot OX11 0FA, UNITED KINGDOM
[4] European Synchrotron Radiation Facility – Institut Laue-Langevin; EPN campus, 71 avenue des Martyrs, 38000 Grenoble Cédex, FRANCE
[5] Université Grenoble Alpes, Laboratoire SIMAP; 101 rue de la Physique, 38402 Saint Martin d'Hères Cédex, FRANCE

1 INTRODUCTION AND BACKGROUND

~~Material scientists~~Metallurgists today have a huge and ~~ever~~ growing array of ~~experimental~~ tools at their disposal for analysis of the materials they are investigating and developing. Traditionally, the approach in this is to study a new material (e.g., alloy chemical composition) and/or manufacturing route (e.g., casting process) by producing samples according to certain specifications and ~~then~~after that characterize ~~their~~the resulting microstructural features and (mechanical) properties so as to identify ~~correlations and ideally~~ relations between those. ~~This is generally referred to as the exploration of microstructure-property relationships and one of the cornerstones of materials science and engineering.~~ The analytical methods for ~~that~~this are thus ~~typically~~ *ex situ* – Latin: "away from the (original) location", or "off-site" – meaning that the synthesis and the analysis are essentially separate ~~events~~activities. The issue with this is that metallurgical mechanisms like crystal nucleation and growth during solidification, recrystallization and texture development during (thermo)-mechanical working, and precipitation sequences and kinetics during heat treatment are assessed on the basis of post-mortem "snap-shots". As a result, ~~any~~ interpretations of these ~~underlying~~ mechanisms are subject to assumptions ~~if not conjectures. Hence this~~and possibly ambiguity. This triggered the development of methods that rather act *in situ* – Latin: "in the (original) location", or "on-site" – to follow events while they ~~are actually occurring~~occur during materials processing. These methods have emerged as very promising ~~analytical~~ means supplementary to the existing ones and giving an actual insight into phenomena as they evolve during for instance casting, hot extrusion and age hardening~~.~~; that is, without these phenomena being masked by those that may occur at a later stage (like phase transformations, formation of intermetallic compounds, and secondary grain growth).

While the category basically covers all methods that monitor events on the spot, this paper is limited to ~~*in-situ* imaging methods and more specifically even to methods that monitor such events using X-rays~~imaging methods and more specifically even to those methods using X-rays. Hard X-rays – by their short wave lengths and high photon energies versus visual light – can penetrate otherwise opaque matter and are therefore used widely to image the inside of objects for medical and security applications, amongst others. This is of interest for metal solidification studies as well, as under appropriate conditions it enables to distinguish solid from liquid phases, and thus the crystals (grains) from the melt. By capturing consecutive images over time, the proceedings can thus be followed *in situ* and without affecting the process. The implementation of techniques designed for this purpose has been pioneered and proved successful as of late.

The results that are ~~introduced~~presented in this paper are outcomes of the ExoMet project, which is a large-scale collaborative research project that is being conducted within the 7th Framework Program of the European Commission [1]. The project (full title: "Physical processing of molten light alloys under the influence of external fields"; duration: June 2012 – July 2016; website: www.exomet-project.eu) targets high-performance aluminum- and magnesium-based materials by exploring grain-refining and nanoparticle additions in conjunction with melt treatment by electromagnetic, ultrasonic and mechanical means. These external fields are to provide for an effective and efficient dispersion of the additions in the melt and their uniform distribution in the as-cast material. The international consortium of companies, universities and research organizations integrates various

disciplines as well as application areas – including automotive, aircraft, and space. Among the project partners, several are engaged in *in-situ* imaging investigations, of which selected examples relating to magnesium-based materials are presented below. The objective of this ~~contribution~~paper is thus to demonstrate how these methods can be used in support of the research and development of such materials.

~~2 ILLUSTRATIVE RESULTS~~

A common aspect in the study of grain-refined and nanocomposite materials is the presence or formation of particles in an alloy melt~~ that~~. These particles are to serve as inoculants for crystal nucleation, or as reinforcements of the solidified matrix~~ material~~, respectively. While ~~particles~~they are typically micrometer- to nanometer-~~size~~sized, their interaction with the alloy during solidification may distinctly affect microstructural development (i.e., as compared to that in the monolithic alloy~~) and by that its observation is of scientific and technological relevance. In this section some results illustrating this point are introduced. To set the scene, each sub-section starts off with a basic introduction, after which the experimental details and obtained results are outlined~~). The case studies below will illustrate this point. To start off with, however, the used materials and methods are introduced.

Formatted: English (United States)
Formatted: English (United States)
Formatted: English (United States)
Formatted: English (United States)
Formatted: English (United States)
Formatted: English (United States)
Formatted: English (United States)
Formatted: English (United States)

~~2~~
2 EXPERIMENTAL PROCEDURES

2.1 Materials

Magnesium is being used for structural applications such as for automotive components because of its weight-saving potential (being 35% lighter than aluminum and 75% lighter than steel). Magnesium alloys are commonly applied as shape castings, using such processes as high-pressure die casting and sand casting for their manufacturing.

To study the solidification behavior with X-ray imaging methods, the contrast between the solid and liquid phases needs to be adequate. This depends on the phases' differences in chemical composition and density. As it happens, this prerequisite is met for the commercial alloy Elektron21, which is a magnesium alloy with rare-earth alloying elements. Alternatively, one may turn to model alloys that contain an alloying element that is just added to provide this contrast, such as zinc. Both options are used in the studies at hand. Ceramic particles generally provide for adequate contrast with a magnesium melt and can be imaged, provided that they are not too small.

2.2 Methods

For the *in-situ* X-ray imaging studies at hand, some distinctly different imaging principles and instruments were used.

Micro-focus X-ray radiography was employed at NTNU Norwegian University of Science and Technology. Figure 1 shows a schematic of the set-up. The laboratory-based configuration consists of a micro-focus X-ray source, a tailored Bridgman-type gradient furnace, and a dedicated X-ray detector [2]. The facility was adapted for the study of

magnesium-based materials by integrating an environmentally controlled chamber to prevent self-ignition of the samples via argon insertion [3]. Samples and their holders are encased between two X-ray transparent glassy carbon plates to avoid any other reactions between molten magnesium and its surroundings. Grain buoyancy and thermo-solutal convection are minimized by orienting the sample cell horizontally; that is, with gravity acting in sample thickness direction. The operating parameters of the X-ray source can be tuned to provide the best compromise between sample transmission and absorption contrast. In a typical solidification experiment, the heating by both elements is adjusted until equi-axed nucleation occurs close to the center of the field of view (FoV), indicating a nearly isothermal condition. A spatial resolution down to 5 µm can be achieved for usual image-capturing rates of 3 Hz. The collected data are subsequently post-processed by means of flat-fielding, noise-filtering and edge-sharpening techniques.

Synchrotron X-ray tomography was employed at Diamond Light Source, UK (Diamond-Manchester imaging beamline I13-2) and at the European Synchrotron Radiation Facility, France (beamline ID19). Figure 2 shows a schematic of the set-up at the latter site. The sample is contained in an argon-filled quartz capillary (to avoid reaction with oxygen and by that self-ignition of the sample), which is fixed on an alumina rod and mounted on a rotating stage. An induction coil is used to heat the samples; the temperature is monitored through a pyrometer and controlled by manually adjusting power supply to the electric generator. The high brilliance of the X-ray source allows for very fast imaging. Thus, numerous projections are recorded by the detector system as the stage rotates, from which afterwards 3D images can be reconstructed by numerical treatment. Details of the two employed tomography set-ups differ somewhat, as is specified in the concerned sub-sections below.

Associated with the differences in the used imaging principles and instruments, there are also differences in the capabilities of the two methods [4]. Where micro-focus X-ray radiography can be implemented as a stand-alone facility and be based for most on commercially available X-ray sources and other components, synchrotron X-ray tomography requires access to one of the few dedicated large-scale facilities. As the names further suggest, radiography provides projections (2D) and tomography provides spatial information (3D).

3 CASE STUDIES

3.1 Solidification of a Mg-Nd-Gd alloy with Zr addition

Formatted: English (United States)

An important class of magnesium alloys uses rare-earth alloying elements for the purpose of enhancing mechanical properties and notably creep resistance. For these alloys, zirconium is commonly added up to saturation level as a potent grain refiner, meaning that it promotes grain nucleation upon solidification which then leads to a correspondingly finer ~~(~~and more favorable~~)~~ microstructure.

Formatted: English (United States)

Formatted: English (United States)

The solidification experiments that are reported here were designed to study the grain-refinement mechanism induced by the presence of zirconium in these alloys ~~by micro~~. Micro-focus X-ray radiography ~~. Interestingly, rare-earth elements in concentrations common~~ was used as it enables multiple experiments to ~~commercial magnesium alloys provide for~~

Formatted: English (United States)

Formatted: English (United States)

~~enough contrast for imaging with this technique, so that actual alloys can~~ be ~~studied rather than model alloys.~~

~~*Materials*~~done to explore the influence of such parameters as cooling rate and ~~*methods*~~ ~~—~~with still sufficient spatiotemporal resolution to distinguish the main morphological features. Two alloy variants based on the Elektron21 alloy were ~~used for the experiments. Nominal alloying contents were~~employed (chemical composition 2.8 wt.% Nd, 1.5 wt.% Gd, balance Mg, which is in line with the commercial equivalent ~~(Nd~2.8 wt.%, Gd~1.5 wt.%),~~ except for the addition of Zn~~.~~). Zr was added in unsaturated and supersaturated concentrations of 0.35 wt.% and 0.86 wt.%, respectively~~, to act as a peritectic precursor. Samples~~. For these experiments at NTNU Norwegian University of Science and Technology, samples were ~~sectioned~~ prepared by sectioning 50×5×1 mm strips from the as-cast ingots ~~into 50×5×1 mm strips~~ , and manually ~~ground~~grind them with progressively finer silicon carbide ~~papers~~paper (up to 4000 grit~~), reaching~~) to reach final ~~sample~~ dimensions of 50×5×0.20(1) mm.

~~—— Then, solidification experiments were carried out at NTNU Norwegian University of Science and Technology, using X-ray radiography to observe microstructure formation. The experimental configuration comprised of a tailored Bridgman type gradient furnace, a micro-focus X-ray source and a dedicated digital camera equipped with a Scint-X scintillator. This setup – described in detail elsewhere [2] – was upgraded for the purpose by integrating an environmentally controlled chamber to prevent self-ignition of molten magnesium via argon insertion (< 0.5% O_2) [3]. The operating parameters for the X-ray source were 40 keV and 50 µA, calibrated by providing the best compromise between absorption contrast and sample transmission. The temperature of the furnace was initially set at 943 K. Subsequently, heater elements were adjusted until equi-axed nucleation occurred close to the center of the field of view (FoV), indicating the establishment of nearly isothermal conditions. Grain buoyancy and thermo-solutal convection were markedly reduced by orienting the radiography sample cell in the horizontal position; that is, with the gravity vector parallel to the small thickness dimension. The role of Zr grain refining particles on α-Mg crystal nucleation was studied at constant cooling rates of 0.0125, 0.05 and 0.1 K/s. Images were recorded continuously during the solidification experiments at a rate of 1 Hz and subsequently post-processed by means of flat-fielding, noise-filtering and edge-sharpening techniques. Solid-area fraction data were extracted for each experimental condition by measuring the solid grain envelopes, which were determined by means of a manually selected global grey level thresholding of the images.~~

~~*Results and discussion*~~

~~—— ~~Figure ~~1 displays~~3 shows the effect of ~~Zr~~zirconium addition level on the ~~nucleation~~development of the α-Mg grains for ~~the distinct~~a relatively low cooling ~~rates~~rate. As time proceeds – and temperature drops – the grains ~~grow~~that appear in bright contrast are growing with a typical six-fold symmetry associated with the hexagonal closed-packed crystal lattice of magnesium. ~~The increase in Zr addition level to well above the peritectic composition leads to an overall increase in~~ In the alloy with high Zr content, the number of nucleation events~~, becoming ~~~ is 1.5–2 times higher than in the alloy with low Zr content. ~~Also, the images confirm that a higher cooling rate enhances nucleation.~~ Upon closer examination of the ~~results~~images for the supersaturated alloy ~~with high Zr content~~, one also detects several dark spots in the ~~regions~~melt just ahead of the solid/liquid interface. ~~The~~

Formatted: English (United States)

Formatted: Font: Not Italic

Formatted: Indent: First line: 0.49"

~~increased X-ray absorption suggests that these~~These could be either pre-existing ~~Zr~~zirconium particles pushed by the growing grains, or new particles forming through a secondary peritectic reaction in the ~~Zr-~~enriched liquid between neighboring grains. Interestingly – despite being several micrometers in size – these particles appear not to promote any further nucleation and are eventually trapped in the eutectic regions ~~surrounding~~between α-Mg grains.

For further comparison, ~~Figure 2 shows the representative Voronoi tessellations for each experimental condition along with the corresponding~~ average grain ~~sizes~~size d after solidification~~. The latter are calculated~~ has been estimated as:

$$d = \left(\frac{6}{\pi N_0}\right)^{1/3}, \quad (1)$$

where N_0 is the grain density~~, namely~~; i.e., the number of ~~grains~~ counted ~~in~~ grains divided by the FoV volume (~~≈~~(~1.11 mm^3). For the alloy with low Zr content, resulting values are 370, 245 and 200 μm for imposed cooling rates of 0.0125, 0.05 and 0.1 K/s, respectively. For the alloy with high Zr content~~ and highest cooling rate, the~~, the matching values are 290, 210 and 170 μm. This confirms that a higher zirconium addition level indeed enhances grain ~~size reaches a minimum~~refinement, as well as that a higher cooling rate leads to finer grains. The last-mentioned grain-size value ~~of ~170 μm, being~~in this set appears to be in ~~reasonable~~fair agreement with earlier grain-refinement efficiency tests using a Mg-Nd-Zn alloy [~~4~~]~~. Also, an increased sensitivity to the~~ 5]. Further, it is to be noted that grain-size dependence on cooling rate is ~~found~~more pronounced for the alloy with the low ~~Zr content~~grain-refiner addition level, similar to results reported earlier for alloys based on the Al-Cu system [~~5~~6].

~~As appears from Figure 3~~ Finally, solid-area fraction data from these experiments are presented in Figure 4. For a given cooling rate, the alloy with high Zr content generally exhibits a higher rate of solid formation than the alloy with low Zr content, which then results in a generally higher solid-area fraction. ~~When~~For the higher cooling ~~rate increases, this remarkable variation takes place~~rates, solidification sets in at ~~increasing~~higher undercooling, ~~which confirms~~suggesting the presence of a higher number of Zr particles becoming potent only if a sufficiently high undercooling is reached. This is in accordance with the so-called Free-Growth model [~~6~~7]. A subsequent decrease in the rate of solid formation is ~~detected~~noted for the alloys solidifying at 0.05 and 0.1 K/s, occurring almost at ~~the~~a same undercooling ~~irrespective of the Zr content; i.e., at ~~~1.25 K and ~~~1.5 K, respectively: no further grain nucleation ~~can be~~is observed in the ~~FoV~~images at these stages. ~~A similar behavior is noted for the~~ The alloy with high Zr content solidifying at 0.0125 K/s~~, giving an undercooling of ~~ behaves similarly, tilting at ~0.7 K. In contrast, the ~~solid area fraction of~~curve for the alloy with low Zr content at this cooling rate evolves ~~following an~~ almost ~~linear trend~~linearly, which can be interpreted as near-equilibrium solidification.

~~2~~3.2 Solidification of a Mg-Zn-Al alloy and its SiC-containing nanocomposite material

One of the main challenges in the melt-metallurgical synthesis of nanocomposites is in achieving a uniform distribution of the particles in the as-cast material. This relates to the introduction of the particles in the melt~~ (where such aspects as wetting, clustering and de-agglomeration come into play),~~ but also to the interaction between particles and the solid-liquid interface during solidification~~ (involving such phenomena as particle pushing and engulfment).~~ As for the latter, the presence of particles may also affect the morphology of the growing grains.

Formatted: Tab stops: 3.15", Centered + 6.3", Right

Formatted: English (United States)

Formatted: English (United States)

Formatted: English (United States)

Formatted: English (United States)

Formatted: English (United States)

The solidification experiments that are reported here were designed to study the effects of nanoparticles on the primary dendritic microstructural evolution. Synchrotron X-ray tomography was used as it enables to capture moving solid-liquid interfaces through reasonably good phase contrast. Material was prepared by blending magnesium alloy AZ91 with pure zinc so as to obtain a model alloy of specific chemical composition (25 wt.% Zn, 7 wt.% Al, balance Mg ~~by synchrotron X-ray tomography~~). Nanocomposite samples were then synthesized by adding 0.7 wt.% SiC powder (average particle size ~25 nm) applying ultrasound to the melt before casting to enhance particle dispersion. For these experiments at Diamond Light Source, ∅1.2 mm cylindrical samples are extracted from the ingots and then encapsulated by graphite and quartz tubes.

Formatted: English (United States)

~~*Materials and methods*~~

~~Material samples containing ~0.7 wt.% SiC powder (average particle size ~25 nm) and a particle-free alloy of the same chemical composition (25 wt.% Zn, 7 wt.% Al, balance Mg) were prepared. The alloy was made by blending magnesium alloy AZ91 with pure Zn through melting and recasting, with the reason for the latter addition being to acquire good imaging conditions with sufficient contrast between the α-Mg crystals and the solute-enriched melt during the solidification. Materials were prepared with identical casting processes and ultrasound-assisted melt processing to enhance nanoparticle dispersion as applicable. From the cast material, ∅1.2 mm cylindrical samples were inserted in a thin graphite tube; then, each tube was further encapsulated in a quartz tube to avoid reaction with oxygen at high temperatures and as such to avoid self-ignition (the graphite tube is to avoid reaction between the molten magnesium and the quartz at high temperatures).~~

~~Then, solidification experiments were carried out at Diamond Light Source, UK, using X-ray tomography to observe microstructure formation. For these experiments, the sample was mounted inside a furnace, with the sample holder being connected to a stage allowing 360° rotation for imaging. The employed image-acquisition system at the used Diamond-Manchester Collaboration imaging beamline (I13-2) comprised of a scintillator which was coupled to a fast PCO® Edge camera through an optical magnification system. This system provides 1.6 μm effective spatial resolution with a 1280×1080 pixel imaging array. A polychromatic X-ray beam of 8–30 keV photon energy range was used. During image capturing, 1200 projections were acquired over a 180° rotation for a single tomogram, with an exposure time of 10 ms per projection (total acquisition time 12 s). The distance between sample and scintillator was set to be ~10 cm. For the experiments, samples were heated to ~665 K (about 30 K above liquidus temperature) and held for 20 min. Then, the furnace cavity containing the sample/crucible was cooled down at a pre-set cooling rate while X-ray projected images were continuously taken until no further changes could be visually observed. Finally, the set of projections for each time step was reconstructed using a filtered back-projection algorithm.~~

~~*Results and discussion*~~

Figure ~~4~~5 shows ~~representative~~ results for the solidification of the monolithic alloy (top) and the composite material ~~at an imposed nominal cooling rate of 0.05 K/s (actual rates varied between 0.035 and 0.06 K/s).~~(bottom). These 2D transverse ~~cross-sections~~slices were constructed from the ~~tomograms~~ 3D tomographic images obtained at distinct points in time, and thus ~~to~~at distinct points during solidification. The cooling rate was set to be quite low to get low growth rates and by that enhance image quality (solid-liquid movement

during the acquisition of a single ~~tomogram~~ tomographic image may induce image blurring). It is to be noted that individual particles as well as actual crystal nucleation ~~events during solidification~~ cannot be recognized due to the limited spatiotemporal resolution ~~of the detection system~~. Further, grains below some micrometers of size will be beyond detection as for the limited absorption difference. The ~~images~~slices at the far left of the figure are those for which first signs of dendrites are ~~first~~ observed~~.~~; these emerge in dark contrast. Upon comparing the ~~cross-sections for the subsequent solidification steps~~chronological images, it ~~seems~~appears that the composite ~~-~~material shows enhanced nucleation ~~but~~and reduced growth ~~rates~~rate versus the monolithic alloy. Smaller average grain size results~~: ~~~ after solidification: 235±35 µm for the ~~nanoparticle-containing sample~~alloy with particles as compared to ~~≈~~300±50 µm for the ~~nanoparticle-free sample~~one without particles. From literature it is known that the α-Mg growth pattern can be remarkably influenced by the characteristics of the surrounding melt [~~7~~8]. That ~~sub-micron size~~submicron-sized particles in a solidifying melt can either be engulfed or pushed by the moving solidification front ~~was also demonstrated by theoretical modeling [8]. This is governed by such parameters as growth rate of the crystals, particle size, viscous drag force, interfacial energy, wettability, and so on. The study indicated that with an increase in particle size, their engulfment by the solidification front tends to decrease. The use of nanoparticles, however, has other implications as well [9].~~is also recognized. Due to their generally poor wettability by a metal melt and their large surface-to-volume ratio, uniform dispersion of ~~individual particles~~nanoparticles is challenging. ~~Agglomeration and clustering are thus~~Clustering is commonly observed and tried to be countered by melt-processing methods such as ultrasonic treatment [9–11]. From ~~the previous~~this it seems reasonable ~~to assume~~ that particle pushing during primary dendritic phase solidification needs to be ~~factored in~~assumed for the ~~solidification~~ experiments at hand. Earlier work also suggests that phase growth can be ~~severely~~ affected by nanoparticle self-assembly ahead of the solidification front [12, 13]. Such accumulation can act as a barrier to diffuse solute (rejected at the solid-liquid interface) away from the advancing solidification front, introducing higher local enrichment close to the solid-liquid interface as compared to regular solidification conditions. That in turn can retard phase growth~~, consistent with the observation in these experiments. Also, low~~. Also, lower solute enrichment in the bulk liquid caused by higher local enrichment close to the solid-liquid interface can permit higher undercooling, increasing nucleation potential. Both mechanisms may lead to microstructural refinement, as observed in the current experiments.

~~Figure 5 presents a comparison of fully solidified samples of the monolithic alloy and the composite material for two distinct cooling rates (0.05 K/s and 0.20 K/s). Microstructural differences between the two materials prove to be consistent for these cooling rates. For the high cooling rate, an overall grain-size reduction is obvious, while differences between the two materials tend to decrease.~~

~~2.3 Re-melting and~~ 3.3 Melting ~~–~~solidification of Elektron21/AlN and Elektron21/Y_2O_3 nanocomposite materials

Interactions between particles and the melt upon solidification ~~are a major concern in the synthesis of nanocomposites, not only because they~~ can apparently affect grain morphology (as ~~noted above~~discussed in the previous case study), but may also ~~because they may~~ lead to

Formatted: English (United States)
Formatted: English (United States)
Formatted: English (United States)
Formatted: English (United States)
Formatted: English (United States)
Formatted: English (United States)
Formatted: English (United States)
Formatted: English (United States)
Formatted: English (United States)
Formatted: English (United States)

non-uniform particle distributions in the as-cast material ~~(~~such as particle clusters on the grain boundaries~~).~~. This also poses the question how these interactions extend and affect eventual material quality when multiple melting ~~an~~and solidification steps are involved, like in recycling.

The ~~re-~~(partial) melting and ~~-~~subsequent solidification experiments that are reported here were designed to study the evolution of particle distribution ~~by synchrotron X-ray tomography – there where their presence at room temperature is masked by intermetallic phases –~~ as well as to detect and observe any ~~potential reaction~~reactions of particles with the melt. ~~Besides checking the efficiency of a particle-dispersion process, the ultimate goal of this type of experiments is to evaluate the interaction of particles with solid/liquid interfaces in a 3D metallic system. Indeed~~As yet, most of the experimental data available on these issues are based on post-mortem observations of quenched samples [14–17~~]~~], or on *in-situ* 2D experiments performed using transparent organic alloys [18–20].

~~*Materials and methods*~~

~~Synchrotron X-ray tomography was used here as it enables 3D real-time observation with actual metallic alloys, thus avoiding potential bias introduced by the experimental limitations in these earlier studies.~~ Two ~~magnesium-based composite~~metal-matrix nanocomposite materials were ~~considered in this study~~employed, both ~~using~~based on the ~~commercial~~ Elektron21 alloy ~~and synthesized by a melt metallurgical route using ultrasound for particle dispersion [21]. Nominal composition of~~. To the base alloy ~~is~~ (chemical composition 2.8 wt.% Nd, 1.2 wt.% Gd, 0.3 wt.% Zn, 0.4 wt.% Zr, ~~0.3 wt.% Zn, and~~ balance Mg~~. Added were~~), either 1 wt.% AlN ~~with an~~ (average particle size ~~of~~ 20–30 nm) or 1 wt.% Y_2O_3 ~~with an~~ (average particle size ~~of ~~~~~~~~500 nm~~. Small cylindrical specimens (diameter ~1 mm, height ~5 mm) were machined from the as-received ingot and introduced into a thin quartz tube (diameter 1.7 mm, wall thickness 0.01 mm) under controlled atmosphere (glove box filled with argon gas with less than 0.1 ppm of oxygen). The capillaries were then temporarily sealed with vacuum grease inside the glove box, extracted and then permanently sealed by melting the quartz tube with a high-temperature torch. The aim of this procedure is to avoid the self-ignition of the magnesium by reducing the oxygen content below the critical reaction threshold.~~

~~Experiments were carried out~~) were added, applying ultrasound to the melt before casting to enhance particle dispersion [21]. For these experiments at the European Synchrotron Radiation Facility, ~~France, using X-ray tomography (beamline ID19).~~ ∅1×5 mm cylindrical samples were machined from the as-received ingot and encapsulated by a quartz tube under argon atmosphere.

Figure 6 ~~shows the experimental set-up, with the capillaries being fixed on an alumina rod (with ceramic glue) and mounted on the rotating stage. An induction furnace was used to heat the samples and perform the experiments. The temperature was monitored through a pyrometer and controlled by adjusting manually the power of the electric generator supplying the inductor. Two tests were carried out: (i) a partial re-melting and -solidification of the Elektron21/AlN composite material, and (ii) a full re-melting and -solidification of the Elektron21/Y_2O_3 composite material. In the first case, the sample was heated at a rate of about ~0.1 K/s until reaching a temperature of ~878 K where the sample is in the semi-solid state. The specimen was then re-solidified at a cooling rate of ~0.1 K/s. In the second case, the sample was brought to the fully liquid state and then re-solidified with a cooling rate of about 1 K/s, which took less than 2 minutes.~~

Formatted: English (United States)
Formatted: English (United States)
Formatted: English (United States)
Formatted: English (United States)
Formatted: English (United States)
Formatted: English (United States)
Formatted: English (United States)
Formatted: English (United States)
Formatted: English (United States)
Formatted: English (United States)
Formatted: English (United States)
Formatted: English (United States)
Formatted: English (United States)

~~Tomography images were acquired regularly during the heating and cooling ramp of the partial re-melting and every 30 s during the full re-~~presents results obtained from a partial melting experiment~~. The beam energy was set to 19.6 keV, the camera was a PCO Dimax and the voxel size was 1.1 µm. The 3D images were made from 800 projections taken over 180° rotation and the time scan was about 1 s for the partial re-melting experiment with a Field of View (FoV) of 816×816×406, and 3 s for the full re-melting experiment with a FoV of 816×816×816. The 3D images were then reconstructed by Paganin reconstruction [22] and processed using the usual image treatments before analysis.~~

Formatted: English (United States)

~~*Results and discussion: partial re-melting experiment*~~

~~Figure 7 presents the microstructural evolution of the~~ on an Elektron21/AlN ~~composite material during re-melting, shown as~~sample. Images (a) and (b) are 2D transverse slices extracted from the 3D tomographic images~~. In the image taken at room temperature~~ in the solid and the partially molten state, respectively. In (a), the rare-earth rich eutectic ~~phase~~ appears in bright contrast while the α-Mg grains appear in dark contrast. ~~Once the temperature exceeds~~ Upon reaching the eutectic temperature, the intermetallic phases located in the ~~inter-dendritic~~interdendritic regions ~~melt (b). The primary phase, on the other hand,~~ start melting. In (b), temperature has further increased, revealing that the α-Mg phase coarsens and its ~~initially~~initial dendritic morphology becomes more globular. ~~By further increasing temperature, some liquid droplets nucleate and grow inside the grains following a mechanism discussed elsewhere [23]. Also,~~Simultaneously the solid fraction ~~decreases~~has decreased and the contrast of the liquid phase ~~becomes~~has become less bright ~~(c). Bright~~. Further, it appears that some liquid droplets nucleate and grow inside the grains, which follows a mechanism discussed elsewhere [23]. Moreover, bright white spots ~~then increasingly appear in the microstructure (c–d).~~emerge as is obvious from (c), which is a larger magnification of the sample at the same temperature. Metallography has revealed that in this composite material the AlN particles are coated by a Zr-rich layer [21], possibly ZrN [24, 25], and mainly appear as micrometer-sized clusters. In some cases, ~~the~~this layer ~~on the particle surface~~ grows into a larger phase, also rich in heavy elements but with a possibly different structure and composition. It is therefore believed that the observed bright white spots ~~observed in the tomographic images~~ are small clusters ~~composed~~ of AlN particles coated by a Zr-rich layer and possibly embedded in a third phase that has grown from the particle surface. The heavy elements in these heterogeneous and compact clusters then act as markers, revealing the presence of the actual AlN particles. From the image ~~(d),~~ it is clear that the particles/clusters are located at the solid-liquid interface as well as within the ~~primary~~α-Mg phase. While it cannot be ruled out that the particles moved from the former to the latter during ~~re-~~melting, this is nevertheless a strong indication that these particles have been there in the as-received state and thus have been engulfed upon initial solidification. The Zr-rich layer on the AlN particles may be instrumental in creating a favorable interface condition for such engulfment. Finally, (d) shows a 3D rendering of the particle distribution in the partially molten state, being indicative for the efficiency of the original dispersion process. The distribution seems fairly uniform at the sample scale, with most particles appearing as micrometer-sized heterogeneous clusters containing heavy elements. As particles in a melt tend to agglomerate in the absence of stirring, it appears likely that particle distribution in the as-received sample has been even more uniform than after its partial re-melting.

~~As shown in~~ Figure ~~8, a 3D rendering of the cluster distribution then gives information on the efficiency of the particle-dispersion process. From this it appears that the spatial distribution is fairly uniform at the specimen scale. Most of the particles appear as micrometer-sized heterogeneous clusters containing heavy elements. The particle/cluster distribution has, however, evolved during the re-melting process. Nevertheless, without external field or stirring the particles generally tend towards agglomeration, so that the distribution in the as-received state will therefore have been only more uniform.~~

~~This composite has shown good mechanical properties and in particular creep resistance [21], but is however not ideal for investigating pushing/engulfment mechanisms. Indeed, additional complexity is introduced as the particles are also reacting with the melt. Figure 9~~7 shows ~~an example~~results from ~~this~~the same experiment ~~where the~~during its successive re-solidification stage. Clearly the bright phase forming from the AlN particle surface grows when it gets in contact with the liquid phase, which is locally enriched in solute. The exact structure and composition of this growing phase is still to be determined. Nevertheless, it is apparent that additional complexity is introduced to the exploration of (nano)-composite materials as particles may be reacting with the melt during their processing.

~~*Results and discussion:*~~ Figure 8 presents results obtained from a full ~~*re-*~~melting and subsequent solidification experiment

~~Among the different alloy/particle systems considered and tested in the framework of the ExoMet project, the~~ on an Elektron21/Y_2O_3 sample, showing 2D longitudinal slices (top) and the corresponding 3D renderings of the particles (bottom) at successive time steps. This particular composite system has proven to be stable; i.e., the ~~Y_2O_3~~ceramic particles do not react in contact with the magnesium-alloy melt. ~~Such system is thus apt for the study of particle interaction with the solidification front.~~

~~Figure 10 presents some initial results obtained for this composite material.~~ After completely ~~re-~~melting the ~~Elektron21~~ matrix (images at ~~time $t=t_0$~~the far left of the figure), most of the particles have ~~sunk to~~settled at the bottom of the sample. ~~Nevertheless~~Yet, some large clusters ~~have~~ ended~~-~~ up at the sample wall (its oxide skin appears bright in these images), so that their interaction with the solidification front ~~upon re-solidification~~ during cooling could be observed. During cooling a thermal gradient was present ~~and the growth front was~~ with solidification progressing from the bottom of the sample to the top ~~(images at times $t=t_0$+30 s, $t=t_0$+60 s, and $t=t_0$+90 s).~~. It appears that some particles are pushed away from the sample wall as the solidification front passes. The observation of large particle clusters being pushed by growing dendrites was recently reported ~~by some of the present authors in~~ for an aluminum~~-alloy [26]. In this composite~~-based nanocomposite material~~,~~ [26]. Here, particle clusters remained in the re-molten state as stable branched networks (coinciding with the ~~clusters were composed of Y_2O_3 particles and oxide films making the aggregate structure hardly breakable.~~original grain boundaries) that turned out to be difficult to break up. In the present case, however, pushing goes along with cluster fragmentation and some ~~individual particles (i.e., the initial micrometer-sized compact clusters)~~ particles are transported far from their original ~~position~~location at the sample wall. ~~These are encouraging results as they open up new possibilities of understanding the interaction of dendritic interfaces with compact particle clusters in a bulk metallic system.~~ Further analyses and additional tests are ongoing to shed light on the mechanisms involved.

Formatted: Font: Not Italic, English (United States)

Formatted: Font: Not Italic, English (United States)

Formatted: Font: Not Italic, English (United States)

Formatted: English (United States)

~~3~~4 CONCLUSION AND OUTLOOK

In this paper it is shown that *in-situ* imaging methods such as micro-focus X-ray radiography and synchrotron X-ray tomography can be used to study microstructural features of magnesium-based grain-refined and nanocomposite materials and local mechanisms involved during their melt-metallurgical processing.

~~For~~Results for one~~, the presented results~~ visualize and by that confirm what is known or assumed. Examples are that magnesium crystals upon solidification grow in a six-fold symmetry, that higher cooling rates during solidification lead to finer microstructures, and that zirconium is a potent grain refiner in magnesium rare-earth alloys. Moreover, they provide for additional insight by enabling to ~~follow~~monitor and quantify phenomena and by that contribute toward a better understanding of the physics at play. Examples are that nanoparticles despite their size can affect the morphology of the growing grains during solidification, that engulfment and/or pushing of particles by the solidification front may or may not occur depending on the specifics of the system, and that chemical reaction at the solidification front may induce the formation of new particles. While the former serves the general understanding and ~~as such~~ can be used for educational purposes, the latter is an enabler for enhancing scientific understanding and supporting technological development ~~and by that~~to be of eventual benefit for industrial applications.

There are restrictions in the use of these methods nevertheless. ~~For~~The number of synchrotron facilities ~~in particular, their number~~ is ~~and will remain~~ limited, so access is a concern along with the need for specific expertise, the long lead times and the limited operational flexibility of the experimental campaigns. Further, concessions may have to be done on alloy compositions (regarding the necessary contrast) and the design of experiments (e.g., at the expense of duplication trials). Nowadays tomography imaging detectors (cameras) with very high acquisition rates are used, leading to huge amounts of collected data, while for other techniques such as diffraction the increasing use of 2D detectors poses a similar challenge. Thus there is ~~a very strong~~an extensive effort to be made on the storage, transfer, processing and analysis of these data. Data management in practice is one of the main concerns, especially in regard of non-expert users. For solidification studies, there still are technical constraints such as on the attainable resolution and field of view of the images versus the features to be studied, and in setting experimental conditions possibly close to those in practice. The former would imply a smaller beam and/or better optics and wider detectors. The latter would imply larger sample ~~volume, meaning higher energy,~~volumes and faster cooling rates, meaning higher energies and higher acquisition ~~frequency~~frequencies (i.e., higher photon ~~flux).~~fluxes), respectively. Developments like these are indeed being considered in topical upgrading programs at existing facilities including the European Synchrotron Radiation Facility.

Recapitulating, for the foreseeable future it is not expected that especially synchrotron studies will become more economical, but faster and more accurate ~~(e.g., by facility upgrades)~~ and only better accessible if post-processing becomes easier. They thus remain to be regarded as high-gain techniques supplementary to those in the metallographical laboratory. In the laboratory, *in-situ* studies will become more common as capabilities of laboratory tomography systems, small-angle X-ray scattering devices and so on further evolve. Moreover, the more "conventional" *ex-situ* characterization techniques

Formatted: English (United States)

Formatted: English (United States)

remain crucial in their own right, ~~as well as~~yet also for the preparation and evaluation of *in-situ* studies.

ACKNOWLEDGEMENTS

The authors wish to acknowledge financial support from the ExoMet project, which is co-funded by the European Commission in the 7th Framework Program (contract FP7-NMP3-LA-2012-280421), by the European Space Agency and by the individual partner organizations. Among the ~~project partners~~consortium, Helmholtz-Zentrum Geesthacht (MagIC), Germany, is thanked for the provision of the magnesium rare-earth testing materials.

~~The work was made possible in part by the facilities and support provided by the~~ Diamond Light Source – Research Complex at Harwell, United Kingdom, ~~funded by~~is acknowledged for the ~~EPSRC (EP/I02249X/1);~~use of the Diamond-Manchester ~~beamline at Diamond Light Source is acknowledged~~ branch-line under ~~proposal~~experiment MT11837-1 and the support from the I13 team. ~~Also the~~The European Synchrotron Radiation Facility, France, is acknowledged for the allocation of beam-time in the framework of the proposals MA-2984 and LTP MA1876~~, as well as~~ and the strong support by the ID19 beamline team ~~for the strong support provided~~.

REFERENCES

1. W.H. Sillekens, D.J. Jarvis, A. Vorozhtsov, V. Bojarevics, C.F. Badini, M. Pavese, S. Terzi, L. Salvo, L. Katsarou, and H. Dieringa, *Metall. Mater. Trans. A*, **45A**, 3349 (2014).
2. A.G. Murphy, D.J. Browne, W.U. Mirihanage, and R.H. Mathiesen, *Acta Mater.*, **61**, 4559 (2013).
3. D. Casari, W.U. Mirihanage, K.V. Falch, I.G. Ringdalen, J. Friis, R. Schmid-Fetzer, D. Zhao, Y. Li, W.H. Sillekens, and R.H. Mathiesen, *Acta Mater.*, **116** 177 (2016).
~~4~~4. C. Rakete, C. Baumbach, A. Goldschmidt, D. Samberg, C.G. Schroer, F. Breede, C. Stenzel, G. Zimmermann, C. Pickmann, Y. Houltz, C. Lockowandt, O. Svenonius, P. Wiklund, and R.H. Mathiesen, *Rev. Sci. Instrum.*, **82**, 105108 (2011).
5. C. Wang, M. Sun, F. Zheng, L. Peng, and W. Ding, *J. Magnesium and Alloys,* **2**, 239 (2014).
~~5~~6. A.G. Murphy, W.U. Mirihanage, D.J. Browne, and R.H. Mathiesen, *Acta Mater.*, **95**, 83 (2015).
~~6~~7. A.L. Greer, A.M. Bunn, A. Tronche, P.V. Evans, and D.J. Bristow, *Acta Mater.*, **48**, 2823 (2000).
~~7~~8. M.Y. Wang, Y.J. Xu, T. Jing, G.Y. Peng, Y.N. Fu, and N. Chawla, *Scripta Mat.*, **67**, 629 (2012).
~~8. J.B. Ferguson, G. Kaptay, B.F. Schultz, P. K. Rohatgi, K. Cho, and C. Kim, *Metall. Mater. Trans. A*, **45**, 4635 (2014).~~
9. R. Casati, *Aluminum Matrix Composites Reinforced with Alumina Nanoparticles*, 1st ed. (Springer, 2016), pp. 9–15, 27–28, 59–72.
10. X. Li, Y. Yang, and X. Cheng, *J. Mater. Sci.*, **39**, 3211 (2004).

Formatted: Font: +Body (Calibri), Not Bold

Formatted: Font: Calibri

11. W. Mirihanage, W. Xu, J. Tamayo-Ariztondo, D. Eskin, M. Garcia-Fernandez, P. Srirangam, and P. Lee, *Mater. Lett.*, **164**, 484 (2016).
12. L. Chen, J. Xu, H. Choi, H. Konishi, S. Jin, and X. Li, *Nat. Commun.*, **5**, 3879 (2014).
13. L. Chen, J. Xu, and X. Li, *Mater. Res. Lett.*, **3**, 43 (2015).
14. F.R. Juretzko, D.M. Stefanescu, B.K. Dhindaw, S. Sen, and P.A. Curreri, *Metall. Mater. Trans. A*, **29**, 1691 (1998).
15. Y.M. Youssef, R.J. Dashwood, and P.D. Lee, *Compos. Part. A: Appl. Sci. Manuf.*, **36**, 747 (2005).
16. T. Lierfeld, P. Gandham, M. Kolbe, T. Schenk, H.M. Singer, G. Eggeler, and D.M. Herlach, *Mater. Sci. Eng. A*, **449–451**, 689 (2007).
17. D.M. Stefanescu, B.K. Dhindaw, S.A. Kacar, and A. Moitra, *Metall. Trans. A*, **19**, 2847 (1988).
18. D.R. Uhlmann, B. Chalmers, and K.A. Jackson, *J. Appl. Phys.*, **35**, 2986 (1964).
19. J.A. Sekhar and R. Trivedi, *Mater. Sci. Eng. A*, **147**, 9 (1991).
20. D.M. Stefanescu, F.R. Juretzko, A. Catalina, B.K. Dhindaw, S. Sen, and P.A. Curreri, *Metall. Mater. Trans. A*, **29**, 1697 (1998).
21. L. Katsarou, M. Mounib, W. Lefebvre, S. Vorozhtsov, M. Pavese, C. Badini, J.M. Molina-Aldareguia, C.C. Jimenez, M.T. Pérez Prado, and H. Dieringa, *Mater. Sci. Eng. A*, **659**, 84 (2016).
22. D. Paganin, S.C. Mayo, T.E. Gureyev, P.R. Miller, and S.W. Wilkins, *J. Microsc.*, **206**, 33 (2002).
23. S. Terzi, L. Salvo, M. Suéry, A.K. Dahle, and E. Boller, *J. Mater. Sci.*, **48**, 7422 (2013).
24. A. Koltsov, F. Hodaj, N. Eustathopoulos, A. Dezellus, and P. Plaindoux, *Scr. Mater.*, **48**, 351 (2003).
25. R.E. Loehman and A.P. Tomsia, *Acta Metall. Mater.*, **40**, S75 (1992).
26. R. Daudin, S. Terzi, P. Lhuissier, L. Salvo, and E. Boller, *Mater. Des.*, **87**, 313 (2015).

Formatted: Justified, Indent: Left: 0", Hanging: 0.39"

FIGURE CAPTIONS

Figure 1 Micro-focus X-ray ~~radiograms~~radiography: experimental set-up in the NTNU home-lab (Viscom Vision Technology XT9100 X-ray source, ① sample, ② heater element, ③ adiabatic zone, ④ field of ~~solidifying~~ view, ⑤ projected image, ⑥ Vosskuhler DXI-11000 CCD camera equipped with a Scint-X scintillator).

Figure 2 Synchrotron X-ray tomography: experimental set-up on the ESRF–ID19 beamline (① sample, ② quartz capillary, ③ alumina rod, ④ rotation stage, ⑤ induction coil, ⑥ pyrometer, ⑦ scintillator, ⑧ optics system, ⑨ PCO Dimax camera).

Figure 3 Microstructural evolution during solidification of Elektron21-based alloys ~~showing the effect of~~ with different zirconium contents C_{Zr} – cooling rate CR=0.0125 K/s (experimental: thermal cycling with cooling from 943 K; imaging: micro-focus X-ray radiography, beam energy 40 keV and ~~cooling rate CR on the nucleation~~50 µA, field of ~~the α-Mg grains.~~view 2,817×1,848 µm, virtual pixel size ~1.4 µm, image-capturing rate 1 Hz).

~~Figure 2 Reconstructed grain-nucleation centers and microstructures of the solidified Elektron21-based alloys for each experimental condition, including the estimated average grain-size values.~~

~~Figure 3~~ Figure 4 Solid-area fraction ~~of the solidifying Elektron21-based alloys~~ in dependence on the undercooling ΔT ~~– measurements are taken every~~ during solidification of Elektron21-based alloys with different zirconium contents C_{Zr} and for different cooling rates CR (experimental and imaging: as for Figure 3, with solid grain envelopes measured using a manual grey-level thresholding of the images).

Figure 5 ~~s for cooling rate CR=0.0125 K/s, with additional data points considered for CR= 0.05 and 0.1 K/s to have more reliable interpolations.~~ Microstructural evolution during solidification of a Mg-25Zn-7Al alloy and a Mg-25Zn-7Al/SiC nanocomposite material – from left to right: at 635 K, at 622 K, at 604 K, at 577 K, and at 532 K (experimental: cooling from ~665 K at 0.05 K/s; imaging: synchrotron X-ray tomography, polychromatic beam, beam energy 8–30 keV, 1200 projections over 180° rotation per tomographic image, exposure time 10 ms/projection, distance sample–scintillator ~10 cm, 1.6 µm effective spatial resolution with a 1280×1080 pixel imaging array).

~~Figure 4 Transverse tomographic cross-sections of a Mg-25Zn-7Al alloy (top) and Mg-25Zn-7Al/SiC nanocomposite material (bottom) upon solidification – from left to right: first crystals appearing at T_0 (~635 K), T_0-12.6 K, T_0-30.6 K, T_0-57.6 K, T_0-102.6 K (all images share the same scale bar).~~

~~Figure 5 Transverse tomographic cross-sections of a Mg-25Zn-7Al alloy (top) and Mg-25Zn-7Al/SiC~~

Formatted: Font color: Text 1, English (United States), Kern at 12 pt

Formatted: Pattern: Clear (Background 1)

Formatted: Font: Calibri

Formatted: English (United States)

Formatted: Font: Calibri, English (United States)

Figure 6 Microstructural evolution during melting of an Elektron21/AlN nanocomposite material ~~(bottom) after full solidification.~~

~~Figure 6 Experimental set-up for performing the *in situ* tomography experiments on the ESRF–ID19 beamline (① quartz capillary filled with argon gas, ② induction coil, ③ alumina rod, ④ encapsulated sample – the arrow represents the synchrotron X-ray).~~

~~Figure 7 Microstructural evolution during re-melting of Elektron21/AlN composite material~~: (a) as-received state at 293 K, (b~~) at 830 K, (c –~~d) ~~at 875 K.~~

~~Figure 8 Particle distribution in a partially re-molten Elektron21/AlN composite material: particle distribution in the~~ semi-solid state at 875 K~~.~~ (experimental: heating at 0.1 K/s; imaging: synchrotron X-ray tomography, beam energy 9.6 keV, 800 projections over 180° rotation, time scan ~1 s, field of view 816×816×406 voxels, voxel size 1.1 µm, Paganin 3D image reconstruction [22]).

Formatted: Justified

Figure ~~9~~7 Particle reaction ~~with the melt~~ during ~~re-~~solidification of an Elektron21/AlN ~~composite~~nanocomposite material: (a) at 873 K ~~(t_0),~~ (b) at 863 K ~~(t_0+120 s),~~ (c) at 841 K ~~(t_0+320 s),~~ (d) at 806 K ~~(t_0+687 s),~~ and (e) solidified state, including a 3D rendering of the phase morphology~~.~~ (experimental: partial melting, then cooling from 878 K at 0.1 K/s; imaging: as for Figure 6).

Figure ~~10~~8 Pushing and fragmentation of particle clusters during ~~re-~~solidification of an Elektron21/Y_2O_3 ~~composite material (t_0: first appearance~~nanocomposite material (experimental: cooling from liquid state at 1 K/s; imaging: synchrotron X-ray tomography, beam energy 9.6 keV, 800 projections over 180° rotation, time scan ~3 s, field ~~of solid) – top 2D vertical slices, bottom 3D rendering of the particles.~~view 816×816×816 voxels, voxel size 1.1 µm, Paganin 3D image reconstruction).